P1: aaa Trim: 174mm × 247mm Top: 0.553in Gutter: 0.747in
CUUK632-10 CUUK632-Watters ISBN: 978 0 521 76573 2 June 26, 2009 21:33

10

Fault populations

Richard A. Schultz
Geomechanics – Rock Fracture Group, Department of Geological Sciences and Engineering, University of Nevada, Reno

Roger Soliva
Université Montpellier II, Département des Sciences de la Terre et de l'Environnement, France

Chris H. Okubo
U.S. Geological Survey, Flagstaff

and

Daniel Mège
Laboratoire de Planetologie et Geodynamique, UFR des Sciences et Techniques Université de Nantes, France

Summary

Faults have been identified beyond the Earth on many other planets, satellites, and asteroids in the solar system, with normal and thrust faults being most common. Faults on these bodies exhibit the same attributes of fault geometry, displacement–length scaling, interaction and linkage, topography, and strain accommodation as terrestrial faults, indicating common processes despite differences in environmental conditions, such as planetary gravity, surface temperature, and tectonic driving mechanism. Widespread extensional strain on planetary bodies is manifested as arrays and populations of normal faults and grabens having soft-linked and hard-linked segments and relay structures that are virtually indistinguishable from their Earth-based counterparts. Strike-slip faults on Mars and Europa exhibit classic and diagnostic elements such as rhombohedral push-up ranges in their echelon stepovers and contractional and extensional structures located in their near-tip quadrants. Planetary thrust faults associated with regional contractional strains occur as surface-breaking structures, known as lobate scarps, or as blind faults beneath an anticlinal fold at the surface, known as a wrinkle ridge. Analysis of faults and fault

Planetary Tectonics, edited by Thomas R. Watters and Richard A. Schultz. Published by Cambridge University Press. Copyright © Cambridge University Press 2009.

P1: aaa Trim: 174mm × 247mm Top: 0.553in Gutter: 0.747in
CUUK632-10 CUUK632-Watters ISBN: 978 0 521 76573 2 June 26, 2009 21:33

populations can reveal insight into the evolution of planetary surfaces that cannot be gained from other techniques. For example, measurements of fault-plane dip angles provide information on the frictional strength of the faulted lithosphere. The depth of faulting, and potentially, paleogeothermal gradients and seismic moments, can be obtained by analysis of the topographic changes associated with faulting. Because the sense of fault displacement (normal, strike-slip, or thrust) is related to the local and regional stress states, fault dip angle and displacement characteristics can provide values for crustal strength and magnitudes of stress and strain in map view and at depth while the fault population was active. Statistical characterization of fault-population attributes, such as spacing, length, and displacement, provides an exciting and productive avenue for exploring the mechanical stratigraphy, fault restriction, partitioning of strain between small and large faults, and the processes of fault growth over a wide range of scales that are useful for defining or testing geodynamic models of lithospheric and planetary evolution.

1 Introduction

Faults on the Earth or other planetary bodies rarely occur as solitary entities. Instead, they occur as members of a set, array, network, or population. In a population, faults display wide variation in their primary characteristics, such as length, displacement, and spacing. However, these characteristics do not occur at random. All of the faults' characteristics depend on one another, so that knowledge of one or two key characteristics can provide insight into the values and relationships among the others.

In this chapter we first define the common fault geometries and then review the stress states in a planetary lithosphere that are associated with faults, using the conditions in the Earth's crust as a reference. We then briefly explore some of the main characteristics of fault populations, again using examples from Earth since these have been investigated in the most detail. Because topographic data are becoming more widely available for planetary fault populations, we show how measurements of the structural topography generated by faulting can reveal information about properties of the faults and of the faulted lithosphere. Last, we show how strains can be calculated for planetary fault populations, and end with a summary of challenges for future work on these exciting issues.

2 Faulted planetary lithospheres

Faults have been documented on nearly every geologic surface in the solar system. Normal faults and grabens are probably the most common and are found on Mercury (Watters *et al*., Chapter 2), Venus (McGill *et al*., Chapter 3), the Moon (Watters and

P1: aaa Trim: 174mm × 247mm Top: 0.553in Gutter: 0.747in
CUUK632-10 CUUK632-Watters ISBN: 978 0 521 76573 2 June 26, 2009 21:33

Johnson, Chapter 4), Mars (Golombek and Phillips, Chapter 5), Europa, Ganymede, and several smaller icy satellites of the outer planets including Tethys, Dione, and Miranda (Collins *et al*., Chapter 7). Thrust faults have been identified on Mercury, Venus, the Moon, and Mars (e.g., Suppe and Connors, 1992; Williams *et al*., 1994; Solomon *et al*., 2008; and chapters in this volume). Strike-slip faults have been identified on Mars (e.g., Schultz, 1989; Okubo and Schultz, 2006b; Andrews-Hanna *et al*., 2008) and on the icy satellite Europa that shows large lateral displacements, such as those found at terrestrial transform plate boundaries (Schenk and McKinnon, 1989; Kattenhorn and Marshall, 2006). Individual dilatant cracks (joints) and deformation bands (Aydin *et al*., 2006; Fossen *et al*., 2007) have both been identified on Mars (Okubo and McEwen, 2007; Okubo *et al*., 2008a) and perhaps Europa (Aydin, 2006), and the presence of subsurface igneous dikes has been inferred on Mars from surface topographic data (Schultz *et al*., 2004). In this chapter we focus on faults on the planets and satellites.

2.1 Definition and geometries of faults

The terminology of geologic structures such as joints, faults, and deformation bands has recently been reassessed and streamlined by Schultz and Fossen (2008). Following this terminology, a **fault** is a sharp structural discontinuity defined by its slip planes (surfaces of discontinuous displacement) and related structures including fault core and damage zones (e.g., cracks, deformation bands, slip surfaces, and other structural discontinuities) that formed at any stage in the evolution of the structure. Commonly associated structures such as drag or faulted fault-propagation folds are associated elements not included in the term fault, although clay smearing or other early forms of strain localization may be included.

Faults rarely occur as single entities but occur in association with other faults (and other structures such as joints, folds, anticracks, and deformation bands) having a range of lengths, offsets, and other related characteristics. A **fault set** is a collection of faults that have some element in common, such as age, length, spacing, type, or orientation. A **fault array** is a fault set in which all faults are genetically related to each other (i.e., same deformational event or rock type). A **fault zone** is a narrow array of relatively closely spaced faults having similar strikes. A **fault system** is a spatially extensive array in which the faults interact mechanically. A **fault population** is a system comprised of all faults having the full range of lengths, spacings, displacement distributions, and other characteristics that record the progressive evolution of the faulted domain. Populations of faults, as well as joints (Segall, 1984a) and deformation bands (Fossen *et al*., 2007), are said to be **self-organizing** (e.g., Sornette *et al*., 1990) in the sense that their physical, geometric, and statistical characteristics evolve with increasing deformation of the

P1: aaa Trim: 174mm × 247mm Top: 0.553in Gutter: 0.747in
CUUK632-10 CUUK632-Watters ISBN: 978 0 521 76573 2 June 26, 2009 21:33

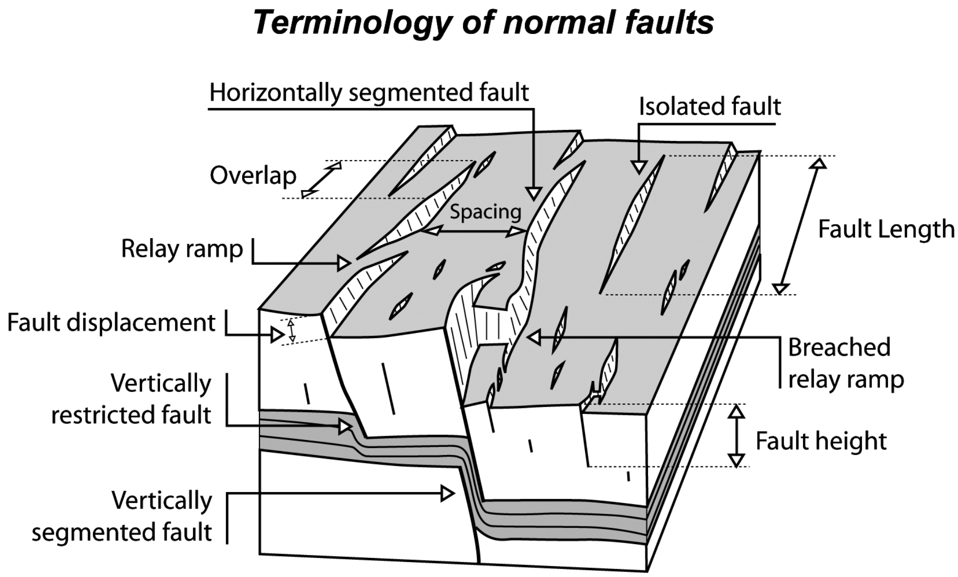

Figure 10.1. Block diagram showing the main geometric characteristics of a surface-breaking fault population. Although normal faults are shown, the descriptions are also applicable to surface-breaking strike-slip and thrust faults on the Earth and other planets and satellites.

region (e.g., Cladouhos and Marrett, 1996; Ackermann *et al*., 2001; Cowie *et al*., 1995).

Fault systems are composed of "isolated faults" and "segmented faults" (Figure 10.1). **Isolated faults** are defined as faults showing no evidence of significant mechanical interaction with other nearby or surrounding faults (Willemse, 1997; Gupta and Scholz, 2000a; Soliva and Benedicto, 2004), i.e., without relay zones or breaching (e.g., Davison, 1994) allowing transfer of displacement to another fault. A **segmented fault** is composed of two or more non-colinear overlapping fault segments that are arranged in echelon patterns (see Davison, 1994). Fault segments are separated by relay zones, or **stepovers** (Aydin, 1988), which are defined as the rock volume between overlapping (echelon) fault tips in which the fault segments interact through their stress fields. This interaction results in a transfer of displacement between the fault segments, an increase of fault-end displacement gradient that is accommodated by continuous deformation, and distortion of the rock volume located between the two fault segments. A fault can be segmented in three dimensions (3-D; vertically and horizontally, Figure 10.1), i.e., containing vertical, horizontal and obliquely oriented relay zones leading to very simplistic (elliptical or rectangular shapes) to more complex fault geometries (Kattenhorn and Pollard, 1999, 2001; Walsh *et al*., 2003; Benedicto *et al*., 2003). A segmented

P1: aaa Trim: 174mm × 247mm Top: 0.553in Gutter: 0.747in
CUUK632-10 CUUK632-Watters ISBN: 978 0 521 76573 2 June 26, 2009 21:33

Table 10.1. *Effective lithostatic stress gradients and rock-mass depths for terrestrial planets*

Planet/Satellite	Gravity, g ($\mathrm{m\,s^{-2}}$)	Dry lithostat σ_v ($\mathrm{MPa\,km^{-1}}$)	Wet lithostat σ_v ($\mathrm{MPa\,km^{-1}}$)	Depth of rock-mass zone, z_0 (km)
Mercury	3.78	10.6	–	2.6–5.2
Venus	8.8	24.6	–	1.1–2.2
Earth	9.8	–	17.6	1–2
Moon	1.62	4.5	–	6–12
Mars	3.7	10.4	6.7	2.6–5.3

Assumes $\sigma_v = \rho(1 - \lambda)gz$ with $\rho = 2800\,\mathrm{kg\,m^{-3}}$ (dry crustal rock). Values calculated and shown where dry or wet conditions can be reasonably inferred. Approximate values for z_0 for Mercury, Venus, Moon, and Mars for the depth range of 1–2 km calculated for depths on those bodies corresponding to σ_v on Earth for dry basalt taken to be at 1–2 km depths.

fault can therefore be composed of fault segments that are breached (connected by cross-faults, or "hard-linked") or not (echelon or "soft-linked"). A linked (formerly segmented) fault is called "**kinematically coherent**" (Willemse *et al*., 1996) because it acts as a single mechanical break.

2.2 Stress states and faulting

The reference stress state for a planetary lithosphere can be inferred from measurements of *in situ* stress within the Earth's crust. Subsurface stresses are, in general, compressive (e.g., McGarr and Gay, 1978; Brown and Hoek, 1978; Engelder, 1993, pp. 10–15; Plumb, 1994; Zoback *et al*., 2003), except perhaps for rare exceptions due to subsurface inhomogeneities (e.g., lava tubes, faults) or for locations close to the surface, where one of the horizontal stresses may be tensile. The vertical stress magnitude, or "lithostat," is given by $\sigma_v = \rho(1 - \lambda)gz$, in which ρ is the average density of rock, λ is the Hubbert-Rubey pore-fluid pressure ratio with $\lambda = P_{water}/\rho_{rock}$ (Hubbert and Rubey, 1959; Suppe, 1985, p. 300; Price and Cosgrove, 1990, p. 68; Weijermars, 1997, pp. 42, 98–99), g is gravitational acceleration at the planetary surface, and z is the depth below the surface (McGarr and Gay, 1978; Zoback *et al*., 2003). Using values of $\rho = 2800\,\mathrm{kg\,m^{-3}}$ and either dry or hydrostatic pore-water conditions ($\lambda = 1/\rho_{rock} \sim 0.4$), as would be the case for the effective principal stresses in the Earth (e.g., Suppe, 1985; Engelder, 1993) and, perhaps at times, for Mars, the calculated lithostats are listed in Table 10.1. These gradients in effective vertical stress σ_v are well documented for the Earth (e.g., Brown and Hoek, 1978; McGarr and Gay, 1978).

P1: aaa Trim: 174mm × 247mm Top: 0.553in Gutter: 0.747in
CUUK632-10 CUUK632-Watters ISBN: 978 0 521 76573 2 June 26, 2009 21:33

Classical rock mechanics treatments suggest values for the minimum horizontal stress of approximately one-third of the lithostatic value based on the Poisson response of an ideal intact linearly-elastic unconfined rock in the horizontal direction (e.g., Jaeger and Cook, 1979; Jaeger *et al*., 2007; see Suppe, 1985, for the "Earth pressure coefficient"). Measurements of *in situ* stress in the Earth's crust demonstrate instead, however, that the magnitudes of the horizontal principal stresses are controlled by the frictional resistance of the fractured planetary lithosphere (e.g., Zoback *et al*., 2003). As originally developed by Goetz and Evans (1979) and Brace and Kohlstedt (1980) in the context of lithospheric strength envelopes for the Earth, the horizontal principal stresses are limited to about one-third to one-fifth of the dry ($\lambda = 0$) or effective ($\lambda > 0$) lithostat, with greater principal-stress differences (or principal-stress ratios) leading to faulting (see Kohlstedt *et al*., 1995, and Kohlstedt and Mackwell, Chapter 9). As a result, the dry or effective principal stresses that drive faulting are all compressive (e.g., Jaeger *et al*., 2007, p. 74), as was shown more than a half-century ago in E. M. Anderson's fault classification scheme (Anderson, 1951; Figure 10.1), so that all three types of faults – normal, strike-slip, and thrust – can be regarded as compressive structures that also shear (see also Sibson, 1974; Marone, 1998; Scholz, 1998).

The critical (minimum) value of the remote (dry or effective) principal stresses for faulting of a planetary lithosphere to be achieved is then given most simply by the Coulomb criterion for frictional slip (Jaeger and Cook, 1979, p. 97; Price and Cosgrove, 1990, p. 26)

$$\sigma_1 = \sigma_c + q\sigma_3, \tag{10.1}$$

in which σ_c is the unconfined compressive strength of the rock mass (Bieniawski, 1989; Schultz, 1995, 1996) and $q = ([\mu^2 + 1]^{0.5} + \mu)^2$ with μ being the average static (or maximum; see Marone, 1998) friction coefficient of lithospheric rocks. Typical values of static and dynamic friction coefficients for crustal rocks on the Earth are $\mu = 0.2$–0.8 (Paterson and Wong, 2005, pp. 166–170; Jaeger *et al*., 2007, p. 70), with strength given by values of static friction at the high end of the range. Setting $\mu = 0.6$ (corresponding to a representative angle of friction for the rock of $\varphi = \tan^{-1}(\mu) = 31^\circ$; see Sibson, 1994), $q = 3.12$ and $\sigma_c = 3.5$ MPa (assuming a typically small value of cohesion for the near-surface rock mass of $C_0 = 1.0$ MPa; see Hoek, 1983; Schultz, 1993, 1996; Hoek and Brown, 1997). Typical ranges of friction coefficient μ of 0.4–0.85 lead to values of $\varphi = 22$–40 and $q = 2.2$–4.68, respectively. For a given value of vertical stress or depth, the maximum (dry or effective) compressive principal stress must be at least 2–5 times larger than the value of the minimum compressive principal stress for normal, strike-slip, or thrust faulting to initiate in a planetary lithosphere. This critical value defines the brittle (Byerlee) frictional strength of planetary rocks having icy or silicate compositions

P1: aaa Trim: 174mm × 247mm Top: 0.553in Gutter: 0.747in
CUUK632-10 CUUK632-Watters ISBN: 978 0 521 76573 2 June 26, 2009 21:33

(e.g., Sibson, 1974; Brace and Kohlstedt, 1980; Kohlstedt *et al.*, 1995; Scholz, 2002, pp. 146–155; Kohlstedt and Mackwell, Chapter 9).

The fault dip angle is related to the friction coefficient (or angle) of the faulted planetary lithosphere. Noting that $q = \tan^2(\theta_{\mathrm{opt}})$, the optimum dip angle θ_{opt} is given by (e.g., Jaeger and Cook, 1979)

$$\theta_{\mathrm{opt}} = \left(45^\circ + \frac{\phi}{2}\right) = \left[90^\circ - \frac{\tan^{-1}\left(\frac{1}{\mu}\right)}{2}\right], \tag{10.2}$$

where θ_{opt} is the angle between σ_1 and the normal to the optimum slip plane. This relationship assumes that one of the (dry or effective) principal stresses is vertical, which is a common occurrence in the Earth (e.g., McGarr and Gay, 1978) and likely in other planets and satellites as well. For a friction coefficient of $\mu = 0.6$ (corresponding to a friction angle $\varphi = 30.5^\circ$), the optimum fault dip angle for a normal fault would be 60.5°; a thrust fault would be oriented according to σ_1 being horizontal, resulting in an optimum dip angle of 29.5°. These values are in accord with the measured dip angles of many large steeply dipping terrestrial faults (Sibson, 1994) that may be modified (either steepened or shallowed) during the progressive deformation of a faulted domain.

At the planetary surface and shallow subsurface, however, faults can dip at initial angles that are steeper than the optimum angle (e.g., McGill and Stromquist, 1979; Gudmundsson, 1992; Moore and Schultz, 1999; McGill *et al.*, 2000; Ferrill and Morris, 2003) because of the pressure and depth dependence of frictional strength in the near surface (e.g., Hoek, 1983; Schultz, 1995) and differences in the initial failure mechanism of near-surface strata (e.g., Gudmundsson, 1992; Schultz, 1996; Peacock, 2002; Crider and Peacock, 2004). Sometimes called the "rock-mass zone" (Schultz, 1993), this region of locally greater effective friction coefficient extends from the planetary surface down to depths of ~1–2 km on the Earth, corresponding approximately to depths on the planets and satellites where the vertical principal compressive stress $\sigma_1 < 10$–35 MPa (with specific values depending on the dry or wet rock density; see Table 10.1). Within this near-surface zone, rock-mass strength is well approximated by the Hoek-Brown criterion (Hoek and Brown, 1980; Hoek, 1983, 1990; Brady and Brown, 1993, pp. 132–135; Franklin, 1993) which is given by

$$\sigma_1 = \sigma_3 + \sqrt{m\sigma_c\sigma_3 + s\sigma_c^2}, \tag{10.3}$$

in which m and s are non-dimensional parameters that describe the friction and degree of fracturing of the rock mass and σ_{c} is the unconfined compressive strength of the intact planetary lithospheric rock material (i.e., its lithology such as basalt or tuff). Values of the parameters are given by the sources cited above, as well as

P1: aaa Trim: 174mm × 247mm Top: 0.553in Gutter: 0.747in
CUUK632-10 CUUK632-Watters ISBN: 978 0 521 76573 2 June 26, 2009 21:33

Schultz (1993, 1995, 1996); the criterion has been applied to planetary faulting by Schultz (1993, 1995, 1996, 2002), Schultz and Zuber (1994), Schultz and Watters (1995), Ferrill and Morris (2003), Schultz *et al*. (2004, 2006), Okubo and Schultz (2004), Neuffer and Schultz (2006), and Andrews-Hanna *et al*. (2008). Stress models for prediction of the types and locations of planetary faults that do not incorporate a criterion for rock-mass strength such as Equation (3) (e.g., Banerdt *et al*., 1992; Freed *et al*., 2001; Golombek and Phillips, Chapter 5) potentially can correctly predict the observed faults (especially strike-slip) when the lithospheric strength is explicitly included (Schultz and Zuber, 1994; Andrews-Hanna *et al*., 2008).

In structural geology, the change in length ΔL between two points in a rock normalized by the original length L_0 between them is referred to variously as the extension, elongation, linear strain, or normal strain. The sign of this quantity, computed by using $\varepsilon_n = \Delta L/L_0$, is positive for an increase in length (extension) or negative for a length decrease (contraction or shortening). In this chapter we refer to ε_n as the *normal strain* (a component of the local strain tensor), following the convention from rock mechanics (e.g., Means, 1976, p. 152; Jaeger *et al*., 2007, p. 43), noting that it applies to penetrative deformation at the particular scale of interest (e.g. Pappalardo and Collins, 2005). For geometrically sparser fault populations, the normal strain ε_n in a given direction (i.e., the horizontal planetary surface normal to fault strike) can be calculated by summing the geometric fault moments as described in Section 5 (see Equation 10.12) below.

Anderson's (1951) classification scheme for faults succinctly associates the three main fault types (normal, thrust and strike-slip) with the 3-D regional stress states needed to drive the required sense of slip along optimally oriented surfaces. Anderson's fault classification scheme is shown in Figure 10.2. With one principal stress vertical (σ_v), the other two are necessarily horizontal (σ_H and σ_h; e.g., McGarr and Gay, 1978; Angelier, 1994). In order of decreasing compressive stress magnitude, the dry or effective principal stresses in a planetary crust are $\sigma_1 > \sigma_2 > \sigma_3$ and $\sigma_H > \sigma_h$. The fault's strike is defined to be parallel to σ_2 (the intermediate principal stress; Sibson, 1974), using the assumption that only the extreme (maximum and minimum) principal stresses are important for driving frictional sliding in a planetary lithosphere (σ_1 and σ_3; e.g., Paterson and Wong, 2005, pp. 35–38). This correspondence between fault strike and σ_2 is commonly observed in nature when the magnitude of normal strain parallel to the fault, ε_2, is negligibly small (i.e., a two-dimensional strain field; see Reches, 1978, 1983; Aydin and Reches, 1982; Krantz, 1988, 1989; Figure 10.2).

For normal faulting, the maximum dry or effective principal stress σ_1 is oriented vertically, denoted the vertical stress σ_v; with the minimum remote dry or effective principal stress σ_h being horizontal (σ_3), the remote stress state for normal

P1: aaa Trim: 174mm × 247mm Top: 0.553in Gutter: 0.747in
CUUK632-10 CUUK632-Watters ISBN: 978 0 521 76573 2 June 26, 2009 21:33

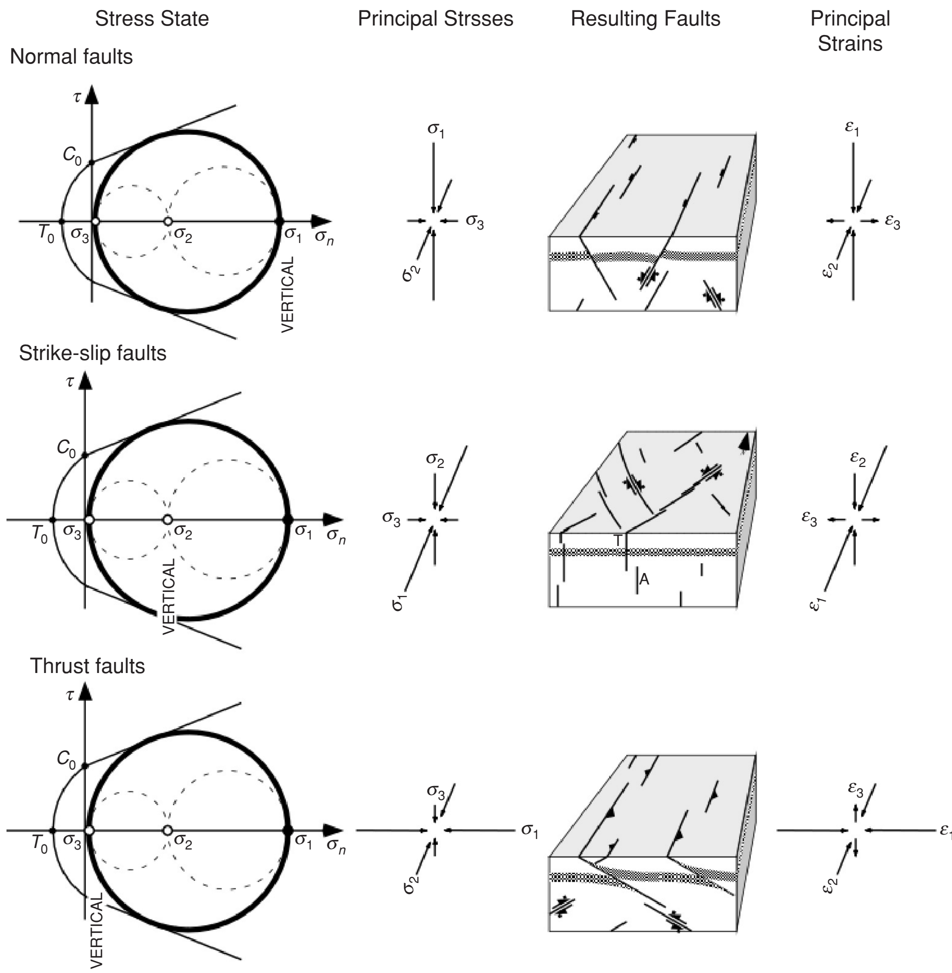

Figure 10.2. The Anderson (1951) classification scheme for faults based on the orientations of the remote (regional) principal stresses relative to the planetary surface. The principal normal strains are also shown (right-hand column); note the change in sign of normal strain ε_1 for extension (normal faults) and ε_3 for strike-slip and contraction (thrust faults). This normal strain, with the opposite sense of the other two, is the "odd axis" of Krantz (1988). Its extensional sense is required when a rock mass deforms with constant volume, as is approximately the case for planetary lithospheres.

faulting and grabens in a planetary crust is given for typical values of friction coefficient ($\mu = 0.6$–0.85) by $\sigma_v = 3$–$5\,\sigma_h$. For thrust faulting, on the other hand, σ_1 is horizontal and σ_3 is vertical, so that $\sigma_H = 3$–$5\,\sigma_v$. For strike-slip faulting, σ_2 is vertical, so that $\sigma_1 = \sigma_H = 3$–$5\,\sigma_h$. Fault sets on a planetary surface are prima facie evidence that the state of stress in a planetary crust was given approximately

P1: aaa Trim: 174mm × 247mm Top: 0.553in Gutter: 0.747in
CUUK632-10 CUUK632-Watters ISBN: 978 0 521 76573 2 June 26, 2009 21:33

by one of these three expressions. The magnitudes of the resulting strains, however, are related to the magnitude of displacement that has accumulated along the faults in the population, as well as the sizes and spatial relationships between the faults (e.g., Segall, 1984a; Gupta and Scholz, 2000b; Schultz, 2003a; see Section 5).

3 Main characteristics of fault populations

The analyses of fault populations began with Earth examples, so the first salient works and main references cited here are for terrestrial fault systems. The characteristics and processes of fault system development (e.g., McGill and Stromquist, 1979; Davison, 1994) described in this section are observed as well in planetary fault systems (e.g., Muehlberger, 1974; Lucchitta, 1976; Sharpton and Head, 1988; Banerdt *et al*., 1992; McGill, 1993; Schultz and Fori, 1996; Mège and Masson, 1996; Schultz, 1991, 1997, 1999, 2000a,b; Koenig and Aydin, 1998; Mangold *et al*., 1998; Watters *et al*., 1998; Wilkins and Schultz, 2003; Okubo and Schultz, 2003, 2006b; Goudy *et al*., 2005; Hauber and Kronberg, 2005; Kattenhorn and Marshall, 2006; Kiefer and Swafford, 2006; Knapmeyer *et al*., 2006), although the rheologies and characteristics of the lithospheric strength envelopes for those bodies differ in detail from the those for the Earth (see Kohlstedt and Mackwell, Chapter 9).

3.1 Fault system morphology

A fault population can be quantitatively described by using a series of geometrical attributes inherent to the fault pattern (see Figure 10.1). Fault *displacement*, i.e., the net slip along the fault (also called the fault "offset"), is an important geometrical attribute since it provides information on fault kinematics and the amount of strain accommodated by the fault. In the absence of three-dimensional data on the fault plane (e.g., Nicol *et al*., 1996; Willemse, 1997; Kattenhorn and Pollard, 2001; Wilkins and Schultz, 2005), the continuous measure of fault displacement along fault trace (the fault's "displacement distribution" or "displacement profile") can be obtained by measuring the displacement of preexisting markers, such as bedding or impact craters, either in a horizontal plane (such as the planetary surface) or in a vertical plane (such as a cross-sectional exposure of the fault; Wilkins and Gross, 2002). On the Earth and other planets and satellites, with many surface-breaking faults but rarer cross-sectional exposures, displacement distributions along the faults' horizontal traces (called the fault "length") are more commonly measured and reported. In addition, however, displacement distributions are generally easier to obtain along normal faults, especially along their horizontal lengths (e.g., Dawers *et al*., 1993), than along strike-slip faults (e.g., Peacock and Sanderson, 1995), for

P1: aaa Trim: 174mm × 247mm Top: 0.553in Gutter: 0.747in
CUUK632-10 CUUK632-Watters ISBN: 978 0 521 76573 2 June 26, 2009 21:33

which horizontal markers would be needed, or thrust faults (e.g., Davis *et al*., 2005), where folding and related deformation can obscure the displacement distribution. This is the reason why fault population analyses have been emphasized for normal faulting environments and also why the following text in this chapter will be based on normal fault populations.

Three other main geometrical attributes used in fault population studies are *length*, *spacing* and *overlap* (Figure 10.1). The **length** of a fault is defined by the distance along the fault trace between the fault tips (where fault offsets decrease to zero) measured along a horizontal surface. Fault **spacing** is the horizontal distance normal to fault strike between two faults. Fault **overlap** is the horizontal distance parallel to fault strike along which two faults overstep (i.e., in the relay ramp between two normal faults (e.g., Davison, 1994; Moore and Schultz, 1999; Schultz *et al*., 2007) or thrust faults (Aydin, 1988; Davis *et al*., 2005), or the length of a pull-apart or push-up range (Aydin and Nur, 1982; Schultz, 1989; Aydin and Schultz, 1990; Aydin *et al*., 1990) along a pair of *en-echelon* strike-slip faults). These geometrical attributes are important for quantitatively describing the geometry of both the relay zones and the overall fault population itself.

Much attention has been devoted to potential measurement biases on these geometrical attributes (e.g., Marrett *et al*., 1999; Ackermann *et al*., 2001; Soliva and Schultz, 2008; and references therein). Two classes of bias can be defined as "natural bias" and "detection bias." Natural bias results from natural geologic processes, such as fault scarp erosion and basin in-filling, that lead to underestimates of fault length, displacement, overlap, and spacing. Detection biases are inherent to the particular data acquisition method (e.g., field photographs, aerial or satellite images, digital elevation models (DEMs); see Priest (1993) for a comprehensive and quantitative treatment of detection biases). Faults with lengths that exceed the dimensions of the measurement area are underestimated, introducing an upper bias referred to as "censoring," whereas image resolution, for example, may lead to undercounting of small faults, introducing a lower bias known as "truncation." Similarly, measurements of fault lengths and displacements are limited by the spatial and vertical resolution of a DEM (e.g., Hooper *et al*., 2003).

The formation of the largest faults and the distribution of strain appear as widely variable in normal fault systems. Two end-member cases can be identified: (1) localized fault systems, with a few large faults accumulating around 50% of the total strain accommodated by the population and a large number of small faults (with a complementary strain) (Figure 10.3a and 10.3c), and (2) distributed fault systems, with strain regularly distributed along evenly spaced faults having a characteristic length scale (Figure 10.3b and 10.3d). These fault system geometries, which are a function of several factors, including deformation rate, stress transmission mode, rheology of the lithospheric strength envelopes including stratification,

P1: aaa Trim: 174mm × 247mm Top: 0.553in Gutter: 0.747in
CUUK632-10 CUUK632-Watters ISBN: 978 0 521 76573 2 June 26, 2009 21:33

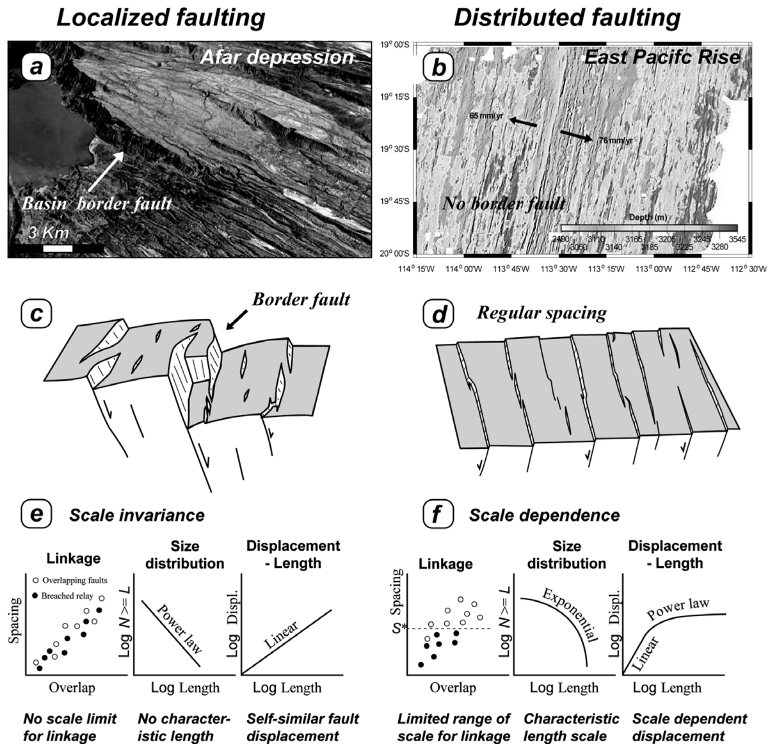

Figure 10.3. Two end-member cases of fault population geometries, after Soliva and Schultz (2008). (a) Normal fault population with localized faulting along relatively few large faults in the Afar depression. (b) Normal fault population from the East Pacific Rise, with distributed faulting along many regularly spaced faults of small and subequal displacement. Figure parts (c) and (d) are schematic views of the fault population geometry of the cases presented in (a) and (b). Figure parts (d) and (e) are the statistical properties specific to each of these cases.

strain magnitude, and properties inherent to the faults and their physical characteristics (see Section 3.3), can be identified and then described precisely by using the fault population statistics.

3.2 Statistical properties

Statistical analysis applied to fault patterns was developed mainly in the 1990s in order to: (1) decipher quantitatively fault and fault-population growth, and (2) predict the fault morphology. For these two reasons, research within the Earth Science community was undertaken to quantify the geometry of faults in as wide a scale range as possible to provide measured dimensions and displacements of faults as tests of various fault growth scaling laws (see summary by Cowie *et al.*,

P1: aaa Trim: 174mm × 247mm Top: 0.553in Gutter: 0.747in
CUUK632-10 CUUK632-Watters ISBN: 978 0 521 76573 2 June 26, 2009 21:33

1996). As mentioned previously, normal fault systems were thoroughly analyzed because of their generally clear expression of the displacement distribution (i.e., topography) along their surface traces.

3.2.1 D–L scaling

The first scaling law studied on multiple fault populations is the *maximum displacement–length* relation ($D_{\max}$–L). Since displacements accumulate along faults during their lateral and down-dip growth, or "propagation," this relation is intended to describe quantitatively, from a simplified mechanical basis, how the faults grow. By analyzing different fault populations separately, the data show that this relation can be explained in log–log space by the following equation (e.g., Scholz and Cowie, 1990; Cowie and Scholz, 1992a,b; Clark and Cox, 1996):

$$D_{\max} = \gamma L^n. \tag{10.4}$$

The parameter γ is called the "scaling factor" (Cowie and Scholz, 1992b) or a "characteristic shear strain" (Watterson, 1986), and the power-law exponent n describes the rate of displacement accumulation relative to L.

The slope of individual fault populations across the full range of lengths and fault types available was shown to be approximately $n = 1.0$ (Scholz and Cowie, 1990; Gudmundsson and Bäckström, 1991; Cowie and Scholz, 1992a; Dawers *et al*., 1993; Schlische *et al*., 1996; Clark and Cox, 1996). Work has also shown, however, that a single relation of the form of Equation (10.4) – with a single unique value of γ – cannot represent all the data from every fault population when all are plotted together (Figure 10.4) (Clark and Cox, 1996; Wibberley *et al*., 1999; Schultz and Fossen, 2002; Soliva *et al*., 2005; Schultz *et al*., 2006, 2008). Instead, each fault population has its own particular scaling law, principally with its own intercept γ that is associated with several factors, including lithology, fault geometry, frictional properties, and stress states. In detail, the distinctiveness of individual fault populations is revealed by variability of the values of γ and n. For example, the variability of these parameters between various fault systems shown from the Earth in Figure 10.3 ($0.538 < n < 2$, and for $n = 1$, $0.0001 < \gamma < 0.6$) suggest that some of the processes acting on fault growth on a given planet or satellite that can modify γ and n are scale dependent, with others related to particular fault geometries within the population (see also Schultz, 1999):

- Host-rock rigidity, as for example soft sediments in the subsurface (Muraoka and Kamata, 1983; Wibberley *et al*., 1999; Gudmundsson, 2004),
- Friction of the fault zone, as for example the transition from deformation band (cm to m scale) to faults (m to km scale) in sandstones (Fossen *et al*., 2007, Wibberley *et al*., 2000),

P1: aaa Trim: 174mm × 247mm Top: 0.553in Gutter: 0.747in
CUUK632-10 CUUK632-Watters ISBN: 978 0 521 76573 2 June 26, 2009 21:33

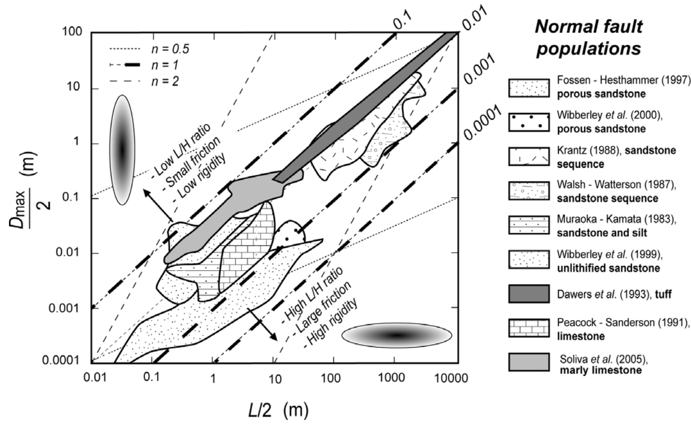

Figure 10.4. Log–log diagram of maximum displacement – length data for terrestrial normal faults, drawn using the convention of $D_{\max}/2$ and fault half-lengths ($L/2$) sometimes used in fault-population studies, following Wibberley *et al*. (1999) and others. Note the wide variation between data groups, especially for small scales. Lines with different exponents n from Equation (3) are reported and labeled. Principal factors that influence the D_{max}/L ratio deduced from field studies and rock fracture mechanics are noted on the diagram including fault aspect ratio (L/H), shown as shaded tipline ellipses.

- Propagation in layered sequences, as for example faults confined to particular layers and vertically restricted by subjacent and superjacent shale layers (Schultz and Fossen, 2002; Wilkins and Gross, 2002; Soliva *et al*, 2005),
- Fault initiation, for example the transition from fracture opening to faulting (Gudmundsson, 1992; Peacock, 2002; Crider and Peacock, 2004), and potentially,
- The rheology of the lithospheric strength envelopes (Cowie, 1998; Bellahsen *et al*., 2003; Soliva and Schultz, 2008).

As a result, the displacement–length scaling relations for a particular fault population can only be understood once the details of fault geometry, interaction and linkage, rock type, mechanical stratigraphy, and geodynamic context are documented and utilized.

3.2.2 Length distribution

Lengths of seismic (earthquake) ruptures were studied in the 1980s and subsequently associated with the faults in order to quantify the long-term fault population strain (e.g., Scholz and Cowie, 1990). One of the main purposes of these early studies was to discuss the relative contribution of larger and smaller faults in the same population, which has implications for strain calculations using remote sensing data from the Earth, as well as from the planets and satellites. A series of measurements of fault populations in the Earth's crust exhibited a negative power-law length distribution on cumulative frequency diagrams (Marrett and Allmendinger,

P1: aaa Trim: 174mm × 247mm Top: 0.553in Gutter: 0.747in
CUUK632-10 CUUK632-Watters ISBN: 978 0 521 76573 2 June 26, 2009 21:33

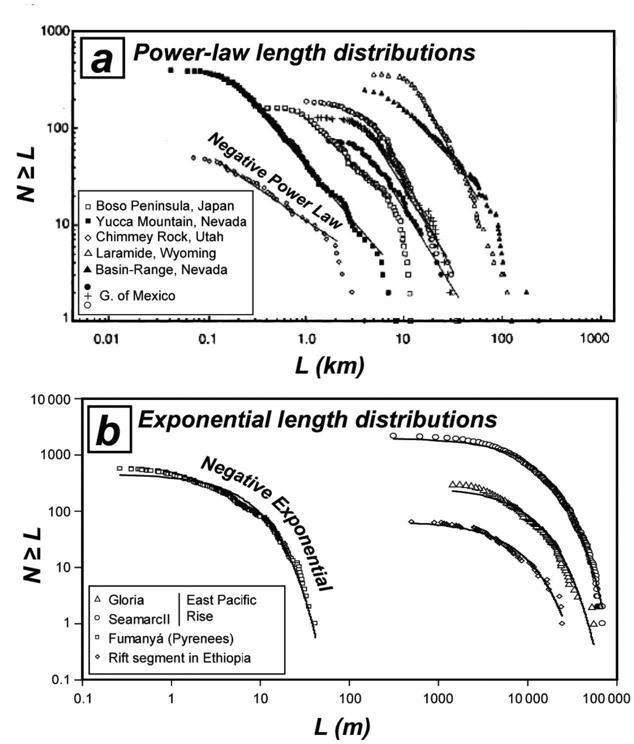

Figure 10.5. Example of characteristic length distributions observed on terrestrial fault populations. (a) Negative power-law length distributions (also called scale-invariant populations). (b) Negative exponential length distributions (scale-dependent populations).

1991; Walsh *et al.*, 1991; Scholz *et al.*, 1993), with a negative power-law exponent, c, varying from ∼0.5 to ∼2 (Figure 10.5a). Similar results were found for Martian fault populations (Schultz and Fori, 1996; Schultz, 2000a). This power-law (or approximately "fractal") distribution reflects strain localized mainly along a few large faults, which themselves contribute up to ∼50% of the population moment and strain accommodation for the case of a typical (and fractal) power-law exponent $c = 2$ (Kakimi, 1980; Villemin and Sunwoo, 1987; Scholz and Cowie, 1990), with the remainder of the moment and strain distributed on the smaller faults in a complementary proportion (Walsh *et al.*, 1991).

This behavior has been interpreted to be the result of the long-term stability and self-similarity of the stress-shadowing process (or elimination process for joints; Aydin and DeGraff, 1988) that controls fault propagation, clustering, and therefore linkage in the whole fault population (see also Cladouhos and Marrett, 1996). However, the assertion that a fault population is self-similar requires a single value of c that remains constant throughout its development, which is not borne out

P1: aaa Trim: 174mm × 247mm Top: 0.553in Gutter: 0.747in
CUUK632-10 CUUK632-Watters ISBN: 978 0 521 76573 2 June 26, 2009 21:33

in nature. Kakimi (1980) suggested that the "fractal dimension" of a given fault population varies with strain magnitude, i.e., have steeper slopes (larger c) when total strains are smaller, and have shallower slopes (smaller c) when total strains are greater, a result verified in numerical experiments by Cladouhos and Marrett (1996), for earthquakes by Wesnousky (1999), and for faults on Mars by Wilkins *et al*. (2002). The variation in the magnitude of fault scaling parameters means that the term "self-similar" may not strictly apply, except perhaps to a particular snapshot of a fault population's development (e.g., see Tchalenko, 1970, for an example).

Alternatively, both field examples and analogue modeling have shown that fault populations involving strain distributed along regularly spaced faults are generally characterized by negative exponential relations and show a characteristic length scale (e.g., Cowie *et al*., 1994; Ackermann *et al*., 2001) (Figure 10.5b). The common aspect of these fault populations is that they grow across a single mechanical layer or unit in which the faults are vertically confined. The confinement of the faults within the layer (also called fault "restriction," e.g., Nicol *et al*., 1996; Schultz and Fossen, 2002) limits the horizontal extent of fault interaction through their stress fields to a nearly constant value (Soliva *et al*., 2006), similar to stratabound joints whose regular spacings scale with the layer thickness (Bai and Pollard, 2000). It appears that the fault population reaches a stage with a characteristic length (Ackerman *et al*., 2001) that can evolve to a maximum length if the layer is "saturated" (Soliva *et al*., 2005), i.e., when the fault spacing stops evolving and the spacing then stabilizes at a constant value.

3.2.3 Spacing

Fault spacing is a sensitive response to the stress field within the fault population (e.g., Cowie and Roberts, 2001; Roberts *et al*., 2004; Soliva *et al*., 2006). Fault spacing, which is dependent on fault displacement magnitude and distribution (Crider and Pollard, 1998; Cowie and Roberts, 2001; Soliva and Benedicto, 2004), is linearly related to fault overlap when the fault-length distributions are described by power laws and when D_{max}–L scaling is linear (i.e., a scale-independent, nonrestricted fault population, Figures 10.3a and 5a; see also Segall and Pollard, 1983, for analogous spacing relationships in nonrestricted joint populations and Olson, 1993, for spacing in restricted joint populations). This fault-length-dependent spacing relationship implies that rocks can support long-term and wide-ranging fault interactions over a broad range of scales (observed from 1 mm to 100 km) (Aydin and Nur, 1982; Peacock, 2003) (Figure 10.6).

On the other hand, fault systems that are characterized by exponential length distributions (Figures 10.3b and 5b) generally show strain distributed along regularly spaced faults (i.e., a lognormal distribution on the length–frequency diagram; e.g.,

P1: aaa Trim: 174mm × 247mm Top: 0.553in Gutter: 0.747in
CUUK632-10 CUUK632-Watters ISBN: 978 0 521 76573 2 June 26, 2009 21:33

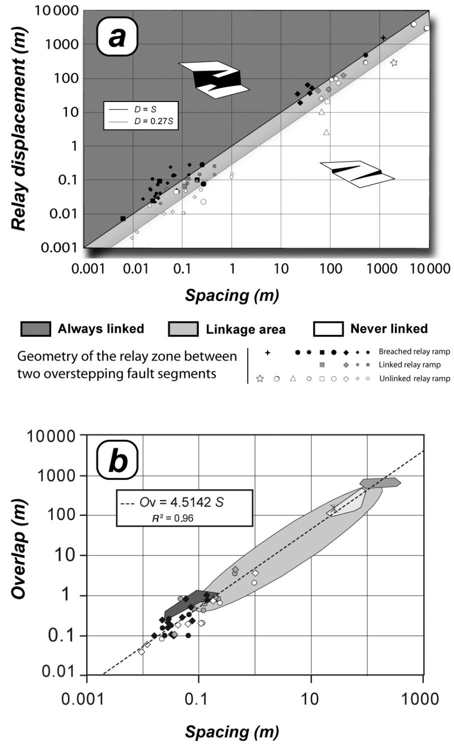

Figure 10.6. (a) Log-log diagram of relay displacement vs. fault spacing, including different published datasets over a large scale range. Gray straight line is the maximum value of relay displacement to separation ratio (D/S) for the data composed only of open relays, with equation labeled. Black straight line is the minimum value of D/S for the data composed of fully breached relay, with equation labeled. (b) Log–log diagram of fault overlap vs. spacing, including different published datasets (gray surfaces) over a large scale range. See Soliva and Benedicto (2004) for the source of data.

Ackermann *et al*., 2001; Soliva and Schultz, 2008; Figure 10.7). As discussed in the previous section, regular fault spacing is due to the limited horizontal extent of the shear stress reduction (or "shadow") zone around the vertically restricted faults that is, in turn, a function of the short and constant fault height in the population (Soliva *et al*., 2006). This effect also limits the maximum distance for strong fault interaction, therefore controlling the dimensions of relay ramps and eventual fault linkage (Soliva and Benedicto, 2004). This behavior is not consistent with self-similar fault segmentation, but instead is related in a scale-dependent manner to the thickness of the mechanical unit in which the faults are confined (see Ackermann *et al*. (2001) and Soliva *et al*. (2006) for normal faults, Schultz and Fossen (2002) for deformation bands, and Hu and Evans (1989) and Bai and Pollard (2000) for joint sets).

P1: aaa Trim: 174mm × 247mm Top: 0.553in Gutter: 0.747in
CUUK632-10 CUUK632-Watters ISBN: 978 0 521 76573 2 June 26, 2009 21:33

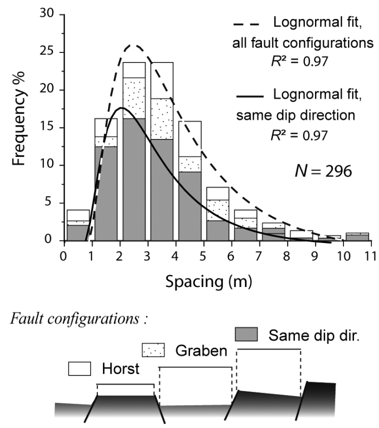

Figure 10.7. Histogram showing the frequency of fault spacing along scan lines crossing a fault population. N is the number of detected intersections between the faults and the scan lines. Spacing between faults having the same dip direction, in horst, and in graben configurations are distinguished. Broken and solid lines are logarithmic-normal fits for all configurations and for faults of the same dip direction, respectively. Least-squares coefficients (R^2) are labeled.

3.3 Mechanisms of fault growth

Fault geometries are frequently analyzed using Linear Elastic Fracture Mechanics (LEFM) (e.g., Pollard and Segall, 1987; Walsh and Watterson, 1988; Pollard and Fletcher, 2005) although some are better matched by using post-yield fracture mechanics (PYFM) (e.g., Cowie and Scholz, 1992b; Schultz and Fossen, 2002) or "symmetric linear stress distribution" (Bürgmann *et al*., 1994; Schultz *et al*., 2006) models. Figure 10.8 summarizes these three quasi-static models. In each of these models, the host rock (taken to be either two-dimensional or three-dimensional in extent) having an approximately homogeneous linear elastic behavior contains a shear displacement–discontinuity (the fault) subject to the far-field, remote, "regional" tectonic stresses and the constitutive relations of the fault (i.e., a constant or variable value of friction along the fault).

In the LEFM model, a constant stress drop (or "driving stress") across the fault produces an elliptical distribution displacement along a straight planar fault, and unrealistically large (infinite or "singular") local stress concentration at the fault tips (Figures 10.8b and c). In the PYFM model, cohesive-frictional end zones are defined that represent the inelastic processes (such as microcracking and fault-tip growth) along and around the fault terminations (Figure 10.8a, see the fault tip). This model therefore integrates the concept of rock yield strength within a larger volume than possible for the LEFM approach, limiting the amount of local stress increase at fault tips to this strength (with values several to several tens of MPa) and

P1: aaa Trim: 174mm × 247mm Top: 0.553in Gutter: 0.747in
CUUK632-10 CUUK632-Watters ISBN: 978 0 521 76573 2 June 26, 2009 21:33

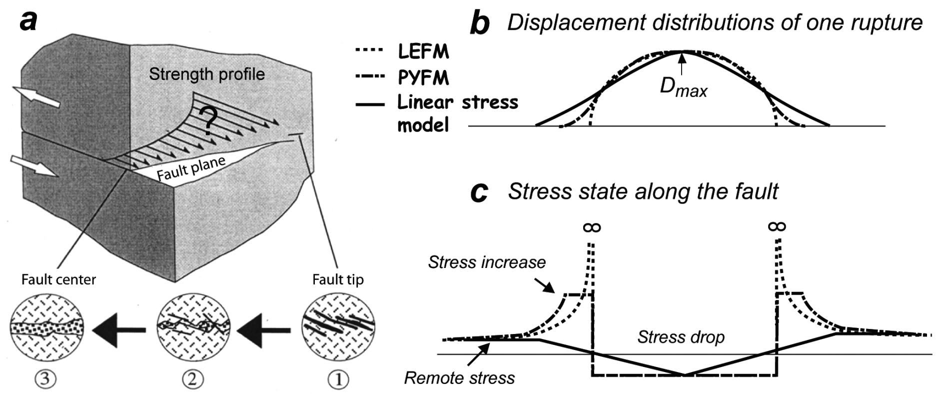

Figure 10.8. Mechanical models of shear rupture along a fault surface. (a) Schematic representation of the fault zone from the tip to the fault center showing the evolution of the fault rock damage and suggesting the evolution of the frictional properties (after Cowie and Scholz, 1992b). (b) Displacement profiles predicted by three mechanical models. (c) Resulting stress distributions along the fault plane. See text for discussion.

producing a bell-shaped displacement distribution along the fault (Figures 10.8b and c; Cowie and Scholz, 1992b; Cooke, 1997; Martel, 1997; Martel and Boger, 1998). In the "symmetric linear stress distribution" model, a linear variation of frictional strength is prescribed along the fault, from a lower value at fault center to a larger value at the fault tips. This approach, which implies a non-constant stress drop along the fault, aims to simulate a variation in constitutive relations, or "maturity," along the fault in which the fault-zone material or gouge is more mature and less resistant to slip near the fault center. This model produces a linear displacement distribution of displacement along the fault, as commonly observed (e.g., Manighetti *et al.*, 2001, 2005), and corresponding patterns of stress changes off the fault as inferred from stress-triggering studies (e.g., Cowie and Roberts, 2001; Roberts *et al.*, 2004) (Figures 10.8b and c).

Work based on these three fault models reveals the importance of four principal sets of parameters:

- Remote stress state
- Host-rock mechanical properties
- Fault geometry
- Friction and the constitutive relations along the fault

The remote stress state in 3-D governs the initial sense of fault displacement (normal, strike-slip, or thrust) and also the displacement magnitude via the differential or driving stress (e.g., Cowie and Scholz, 1992b; Bürgmann *et al.*, 1994). It therefore exerts a primary influence on the average value of $D_{\max}/L$ for a given

P1: aaa Trim: 174mm × 247mm Top: 0.553in Gutter: 0.747in
CUUK632-10 CUUK632-Watters ISBN: 978 0 521 76573 2 June 26, 2009 21:33

fault population (Schultz and Fossen, 2002; Schultz *et al*., 2006). However, the remote stresses are frequently difficult to estimate for inactive fault populations or from planetary observations, and they can be estimated only in a few terrestrial cases where outcrop conditions allow measurements of parameters such as 3-D fault geometry, friction, and material properties (e.g., see Scholz, 2002).

Material properties of the rock surrounding a fault, such as its stiffness or rigidity (as expressed principally by its Young's or shear moduli), near-tip yield strength (Scholz and Lawler, 2004), and viscosity (Bellahsen *et al*., 2003), are also key factors that modulate fault displacement (Walsh and Watterson, 1988; Cowie and Scholz, 1992b; Bürgmann *et al*., 1994; Wibberley *et al*., 1999; Gudmundsson, 2004). This is particularly due to the wide variety of rock mechanical properties that promote a large range of possible values for rocks (e.g., shear modulus, $0.5\,\text{GPa} < G < 50\,\text{GPa}$, from laboratory testing (Hatheway and Kiersch, 1989).

Fault tipline (the line defined by fault surface termination, i.e., where displacement equals zero; Davison, 1994) geometry is an important characteristic that also controls displacement distribution and magnitudes (Cowie *et al*., 1992b; Willemse, 1997; Schultz and Fossen, 2002). Moreover, the morphology of the fault surface is also important. For example, corrugations of the fault surface resulting from rock heterogeneity or fault linkage during its evolution (e.g., Schultz and Balasko, 2003; Okubo and Schultz, 2006a) can permit, or inhibit, displacement with respect to the slip direction (conservative and non-conservative barriers, respectively, in the sense of King and Yielding, 1984).

Fault friction can be thought of as a function of the normal stress and friction coefficient for the fault surface and has been integrated into all three fault growth models discussed above (Figure 10.8c). These models are largely consistent with field observations that show variations in meter-scale fault segmentation geometry, cataclastic fault-rock textures, and fault-rock type from the tips to the center of a fault (e.g., Caine *et al*., 1996; Wibberley *et al*., 2000) (Figure 10.8a). Frictional resistance (friction coefficient times the normal stress, plus cohesion if any) along faults modifies the displacement magnitude and can affect the displacement distribution along a fault (e.g., Aydin and Schultz, 1990; Schultz and Aydin, 1990; Aydin *et al*., 1990; Schultz, 1992; Kattenhorn and Pollard, 1999; Figure 10.8b). Based on these models and fault rock observations, it can be concluded that in porous siliciclastic rocks friction can influence the slope of the $D_{\max}$–L scaling relation for some fault sets (Bürgmann *et al*., 1994; Wibberley *et al*., 1999). Because the magnitude of normal stress resolved on fault planes is related to planetary gravity g, the scaling relations for fault populations on other planets and satellites (having smaller values of g than Earth) differ systematically in the value of their scaling intercepts γ throughout the solar system (Schultz *et al*., 2006), as discussed below. Other potential factors such as far-field extension rate (in terrestrial oceanic

P1: aaa Trim: 174mm × 247mm Top: 0.553in Gutter: 0.747in
CUUK632-10 CUUK632-Watters ISBN: 978 0 521 76573 2 June 26, 2009 21:33

fast- vs. slow-spreading centers or continental rifts) or modes of slip event accumulation (Gutenberg-Richter vs. "characteristic," e.g., Wesnousky, 1994, 1999; Scholz, 2002) are probably of importance for fault population development but are not yet clearly demonstrated with planetary examples and theory.

3.3.1 Fault slip and 3-D propagation

Propagation of a fault requires a critical value of near-tip displacement gradient leading to an amount of fault-tip stress equal to the rock's local yield strength (Cowie and Scholz, 1992b; Bürgmann *et al.*, 1994; Gupta and Scholz, 2000a; Scholz and Lawler, 2004). If the near-tip stress reaches the shear yield strength, the rock fails there by macroscopic shearing, and displacement accumulates along the various parts of the lengthening fault. LEFM models predict an infinitely large value of near-tip stress at the tip of a fault (Figure 10.8) and unambiguously predict a scaling exponent of $n = 0.5$ that is inconsistent with the data compiled in Figure 10.4 (Scholz, 2002, p. 116; Olson, 2003; Schultz *et al.*, 2008).

The two other classes of fault-growth models discussed above (PYFM and the symmetric linear displacement model; Figure 10.8) are consistent with a linear D_{max}–L scaling ($n = 1$) because they avoid producing a near-tip singularity. In these two models, γ is a function of (1) elastic properties; (2) driving stress; (3) yield shear strength; and (4) fault aspect ratio (L/H; see Figure 10.1). These approaches, implicitly or explicitly, consider "radial" or "proportional" fault growth (fault propagation having approximately the same rates down-dip and horizontally) and predict a range of fault displacement profiles from bell-shaped to linear (Figure 10.8b). The growth of such an isolated fault can produce nearly circular or elliptical tipline shapes (e.g., Nicol *et al.*, 1996; Martel and Boger, 1998) if the rock strength is comparable around the fault tipline. In layered rocks, H can remain constant during fault growth if the tipline is restricted by a lithologic or rheological barrier (i.e., "vertical restriction" in Figure 10.1) (Scholz, 1997; Schultz and Fossen, 2002). In this case, the slope of the fault-population exponent changes from $n = 1$ in the earlier, non-restricted, proportional growth phase, to $n < 1$ as the faults grow laterally while being restricted vertically (Schultz and Fossen, 2002; Soliva *et al.*, 2005; Fossen and Gabrielsen, 2005, p. 161; Figure 10.4).

3.3.2 Interaction and linkage

Fault interaction and linkage are a major process leading to fault growth (Peacock and Sanderson, 1991; Dawers and Anders, 1995; Mansfield and Cartwright, 1996; Crider and Pollard, 1998; Cowie and Roberts, 2001). Field data and theory have shown that two initially isolated fault segments can interact through their stress fields as they grow, eventually linking across their relay zones in 3-D (e.g., Segall and Pollard, 1980; Figures 10.9a,b and c). During the first step of fault interaction,

P1: aaa Trim: 174mm × 247mm Top: 0.553in Gutter: 0.747in
CUUK632-10 CUUK632-Watters ISBN: 978 0 521 76573 2 June 26, 2009 21:33

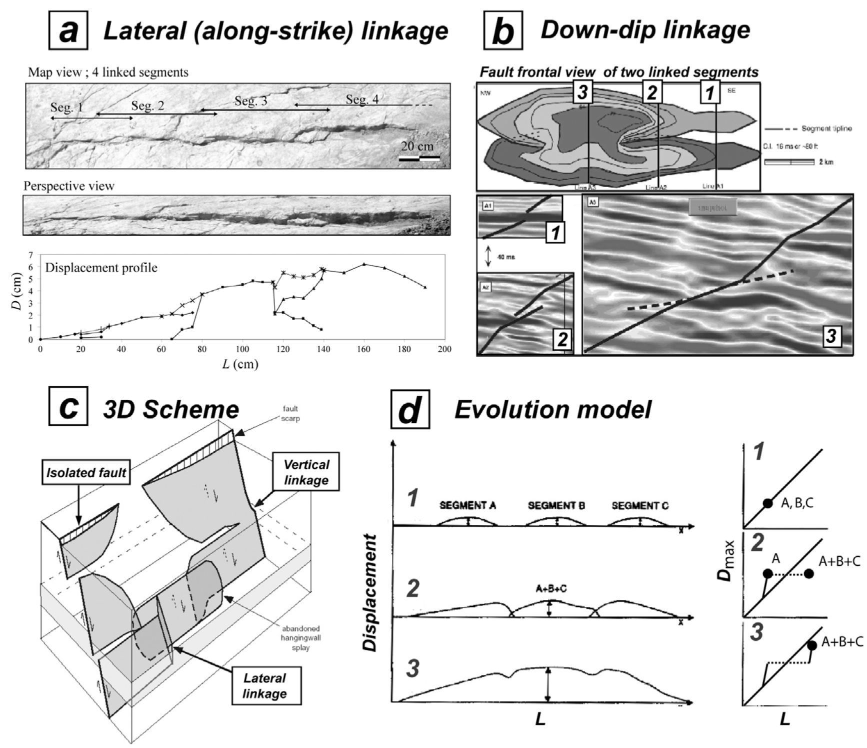

Figure 10.9. 3-D geometry and evolution of segmented normal faults. (a) Geometry of lateral linkage and associated displacement distribution. (b) Three-dimensional (3-D) geometry of vertical linkage and associated 3-D displacement distribution. (c) 3-D representation of segmented faults. (d) Displacement evolution model.

the increase of shear stress around the stepover, or relay zone, leads to a transfer of displacement on one or each segment if both are actively slipping, leading to an increase of displacement gradient along the interacting fault ends. This interaction promotes an increase of the D_{max}/L ratio, which ultimately can lead to an abrupt increase in length by linkage of the temporarily over-displaced fault segments and a subsequent period of fault displacement recovery for the newly linked fault (Figure 10.9d). When fault linkage and displacement readjustment are achieved, the resulting linked segmented fault can behave as a new larger kinematically coherent fault having a D_{max}/L ratio consistent with non-linked isolated faults (e.g., Cowie and Roberts, 2001). These perturbations of fault displacement, due to the short-range mechanical interactions between the closely-spaced fault segments, can explain a large component of the scatter observed on D_{max}–L diagrams (Figure 10.4). Fault interaction and linkage also control other fault population characteristics, such as: (1) fault length distribution (Cladouhos and Marrett, 1996),

P1: aaa Trim: 174mm × 247mm Top: 0.553in Gutter: 0.747in
CUUK632-10 CUUK632-Watters ISBN: 978 0 521 76573 2 June 26, 2009 21:33

(2) fault spacing (Soliva *et al*., 2006), geometry of syntectonic basins and deposits (e.g., Gawthorpe and Hurst, 1993), and (3) slip and sedimentation rate (e.g., Ravnas and Bondevic, 1997; Cowie and Roberts, 2001).

3.3.3 Whole fault system development

The compiled datasets shown in Figure 10.4 give a synoptic view of the D_{max}–L scaling relationships of normal faults observed at the Earth's surface. These data show a scatter of the D_{max}/L ratio (from 10^{-3} to 4×10^{-2}) for faults of $L < 200$ m. This suggests that at a small scale (relative to the mechanical unit thicknesses typical of stratified igneous or sedimentary sequences), fault displacement is greatly influenced by both the lithological discontinuities (acting on fault shapes) and the rheology (stiffness or rigidity, friction) of each rock type. This wide D_{max}–L variability is possible because of the small dimension of the faults with respect to the mechanical unit thicknesses, allowing the faults to be sensitive to the specific rheology of each mechanical unit. In contrast, if the fault dimension is large enough with respect to the lithological stratification (for example 1 km long for mechanical units of meter-scale thickness), displacement must then be controlled by the average rheology of the entire bounding layered sequence. This seems to be a reasonable explanation for at least some of the scale dependence of the D_{max}–L data variability (e.g., Soliva *et al*., 2005; see the large scatter for small faults compared to large faults in Figure 10.4). Therefore, regardless of the fault initiation process (see Crider and Peacock, 2004) or other factors such as propagation rates (e.g., Walsh and Watterson, 1987; Peacock and Sanderson, 1996), it is improbable that a fault will grow with a consistently linear D_{max}–L behavior (i.e., without change of slope) from the centimeter to the kilometer scale in layered sequences of contrasting lithologies.

To understand fault population growth and scaling, Gupta and Scholz (2000a) calculated the perturbation of the maximum Coulomb shear stress (King *et al*., 1994; Harris, 1998) around a series of faults. They showed that interaction and subsequent linkage develop preferentially for similar spacing/overlap ratios independent of the scale of observation, where D_{max}–L scaling, fault aspect ratio, and the tipline geometry are scale invariant. Their work suggests that a self-similar segmentation geometry is mechanically possible in a fault population if the shear stress perturbation around the faults scales linearly with their horizontal lengths. This self-invariant process of linkage allows the formation of very large faults by linkage of smaller growing segments (e.g., Cowie *et al*., 1995), therefore allowing large strain localization along just a few faults (corresponding to the first end-member case discussed above, Figure 10.3a). The increase of fault size (1) increases the rock volume of reduced stress that shadows the activity of smaller faults, and (2) allows the development of the largest faults, which promotes an approximately

P1: aaa Trim: 174mm × 247mm Top: 0.553in Gutter: 0.747in
CUUK632-10 CUUK632-Watters ISBN: 978 0 521 76573 2 June 26, 2009 21:33

fractal geometry (or scale-invariant negative power-law length distributions) of the fault population (Sornette *et al*., 1990; Cladouhos and Marrett, 1996).

Because rock-mass characteristics such as rheological contrasts in layered stratigraphies can control the geometry of one fault, it can therefore control fault interactions throughout the entire fault population (e.g., Soliva *et al*., 2006). The population can thereby change from localized to distributed strain (e.g., see the two end-member cases shown in Figure 10.3). This case concerns populations of active faults that are confined within a layer of given thickness. Here, faults grow horizontally with their vertical extent being limited, or restricted, by adjacent layers that act as mechanical barriers (e.g., Scholz, 1997), leading to regularly spaced faults. In this regime, faults are no longer self-similar in displacement distribution since they are vertically restricted, and instead generally exhibit flat-topped displacement profiles (Ackermann *et al*., 2001; Soliva *et al*., 2006). The scaling of restricted faults is well explained by non-linear growth paths on the D_{max}–L diagram (i.e., 3-D PYFM conditions with constant fault height; Schultz and Fossen, 2002; Soliva *et al*., 2005; Figure 10.10c). This growth sequence has been observed in fault populations over a wide range of scales and structural contexts (Cowie *et al*., 1994; Carbotte and Macdonald, 1994; dePolo, 1998; Poulimenos, 2000; Manighetti *et al*., 2001; Bohnenstiehl and Carbotte, 2001; Polit, 2005; Soliva and Schultz, 2008; Polit *et al*., 2009). Cowie *et al*. (1994) describe crustal-scale fault populations in oceanic lithosphere at the East Pacific Rise and Soliva and Schultz (2008) along the Main Ethiopian Rift, where the much of the strain is distributed on nearly evenly spaced faults (Figure 10.5b). At the East Pacific Rise, the fault population has been interpreted to indicate growth within (confined to) the oceanic brittle crust (Cowie, 1998; Bohnenstiehl and Kleinrock, 1999; Garel *et al*., 2002), whereas at the Main Ethiopian Rift the faults seem confined to competent basalts. These faults also show non-linear D_{max}–L scaling with a significant decrease in the D_{max}/L ratio with increasing fault length, i.e., $n < 1$ (Cowie *et al*., 1994; Manighetti *et al*., 2001).

3.4 Scaling relations for planetary faults

Precision measurements of the maximum displacement ("offset," D_{max}) and map lengths L of surface-breaking faults on Mars and Mercury demonstrate that less displacement per unit length is accumulated along faults on these planets than along terrestrial ones. For example, normal faults from Tempe Terra (Mars) and thrust faults from Arabia Terra (Mars) show D_{max}/L ratios of 6.7×10^{-3} (Wilkins *et al*., 2002; Watters, 2003) and 6×10^{-3} (Watters *et al*., 1998), respectively. Thrust faults from Mercury also show D_{max}/L ratios of 6.5×10^{-3} (Watters *et al*., 2000, 2002; Watters and Nimmo, Chapter 2). The fault populations discussed here currently lack

P1: aaa Trim: 174mm × 247mm Top: 0.553in Gutter: 0.747in
CUUK632-10 CUUK632-Watters ISBN: 978 0 521 76573 2 June 26, 2009 21:33

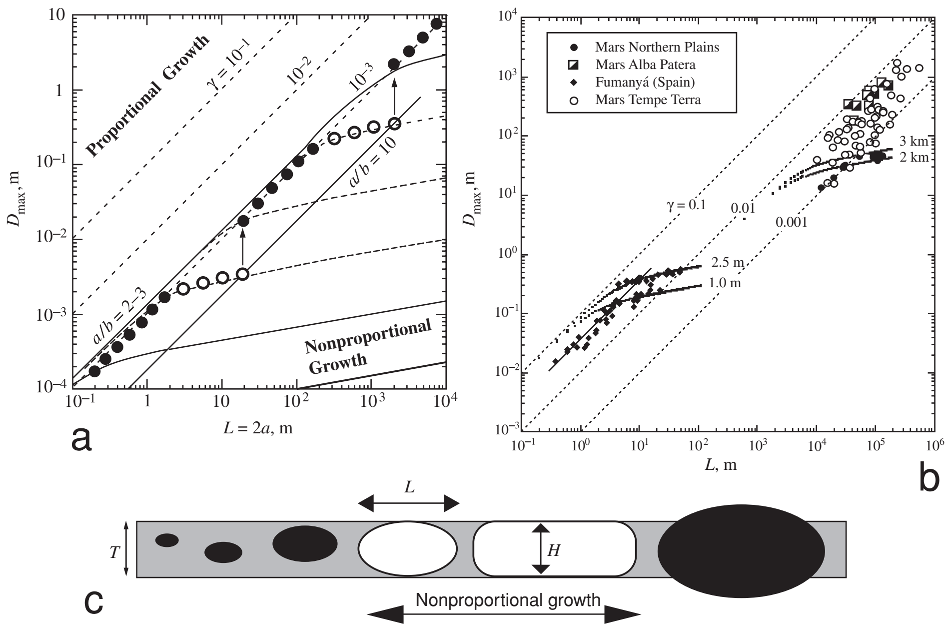

Figure 10.10. 3-D displacement–length scaling relations and the growth of stratigraphically restricted faults. (a) Fault growth paths on the D_{max}–L diagram (after Schultz and Fossen, 2002) showing stair-step trajectory of alternating proportional (linear, filled symbols) and non-proportional (restricted, open symbols) fault growth. (b) Examples of restricted fault populations on Earth (normal faults from Fumanyá in the southeast Pyrenees, after Soliva *et al*., 2005) and Mars (graben-bounding normal faults from the northern plains, after Polit, 2005, and Polit *et al*., 2009). (c) Cross-sectional fault geometries shown schematically for each part of the growth sequence. Filled and open symbols for fault-shape ellipses as in (a).

evidence for significant restriction, although many of their characteristics such as displacement distributions that could suggest restriction remain to be investigated; in contrast, a set of restricted grabens from the Tharsis area of Mars (Polit, 2005; Polit *et al*., 2009) are discussed below (see Figure 10.10c). Typical values for terrestrial faults (normal, strike-slip, or thrust) are $\sim$1–5 $\times 10^{-2}$ (see the recent compilations by Schultz *et al*., 2006, 2008). Currently, topographic data of sufficient accuracy and resolution to assess D_{max}–L scaling of faults are available only for Mars and Mercury.

The data for Martian normal faults, such as those on Tempe Terra (Wilkins *et al*., 2002), are systematically offset to smaller values of displacement by a factor of about five from the terrestrial data (Figures 10.10b and 10.11a). A similar offset is observed for thrust faults on both Mars and Mercury (Plate 25b). Detailed examination of the Martian and Mercurian faults indicates that the smaller D_{max}/L

P1: aaa Trim: 174mm × 247mm Top: 0.553in Gutter: 0.747in
CUUK632-10 CUUK632-Watters ISBN: 978 0 521 76573 2 June 26, 2009 21:33

ratios result from smaller displacements (accurately measured from topographic data; e.g., Watters *et al.*, 1998, 2000, 2002; Wilkins *et al.*, 2002) rather than an overestimation of fault lengths by the same factor of five.

Schultz *et al.* (2006) found that the $D_{\max}/L$ ratio for non-restricted faults depends on three primary factors: stiffness of the rock surrounding the faults (Young's modulus or shear modulus (rigidity)), shear driving stress, and yield strength, with all three of these primary factors being influenced to various degrees by planetary gravity g. For the same conditions of rock type (e.g., basaltic rock mass), fault type (normal), and fluid-saturated crustal rocks (i.e., "wet" conditions with $\lambda = 0.36$–0.4), g reduces $D_{\max}$ for Martian faults, relative to terrestrial ones, by $g_{\text{Mars}}/g_{\text{Earth}} = 0.38$ (via the driving stress term). Yield strength in shear scales with gravity, with the strength of the Martian basaltic rock mass being approximately one-half of the corresponding terrestrial one. Modulus decreases with decreasing g, to a normalized value of $\sim$0.84 for the (wet) Martian case. The combined effect of g on all three key factors is a reduction in $D_{\max}/L$ of about a factor of 5–6, consistent with the data for normal and thrust faults from the literature (e.g., Clark and Cox, 1996; Schultz *et al.*, 2006).

Restricted faults have only recently been recognized in planetary datasets (Figure 10.10b) and the implications of this class of fault for the stratigraphy, seismology, and tectonics of planets and satellites is as important for those bodies as for the Earth itself (see discussion by Knapmeyer *et al.*, 2006). Fault restriction can be identified in terrestrial and planetary datasets by using one or more diagnostic techniques, including quantitative examinations of the fault-related topography (Soliva *et al.*, 2005; Polit *et al.*, 2009), spacing (e.g., Soliva *et al.*, 2006), $D_{\max}$–L ratios (e.g., Soliva and Benedicto, 2005; Polit *et al.*, 2009), relay-ramp dimensions (e.g. Soliva and Benedicto, 2004), and length–frequency data (e.g., Gupta and Scholz 2000b; Soliva and Schultz, 2008). Stratigraphically restricted faults represent snapshots of the progressive growth of fault systems in layered sequences and their strain magnitudes can be computed by using the well-known equations for "large faults" (see Section 5).

Assessment of $D_{\max}$–L scaling relations of faults on the Moon, Venus, and icy satellites of the outer solar system is currently hindered by large uncertainties in measurements of displacement (due to low-resolution, or unavailable, topographic data) and, to a lesser extent, length (due to imaging data having coarse spatial resolution). The results summarized here (Figure 10.11) suggest that faults on Venus (see McGill *et al.*, Chapter 3) should accumulate somewhat smaller displacements than their terrestrial counterparts given an $\sim$10% reduction in gravity ($g = 8.8\,\text{m}\,\text{s}^{-2}$) relative to the Earth. Faults on the icy satellites of Jupiter and Saturn (see Collins *et al.*, Chapter 7) probably also scale with gravity, with particular values of the $D_{\max}/L$ ratio depending on appropriate values of near-tip ice strength and

P1: aaa Trim: 174mm × 247mm Top: 0.553in Gutter: 0.747in
CUUK632-10 CUUK632-Watters ISBN: 978 0 521 76573 2 June 26, 2009 21:33

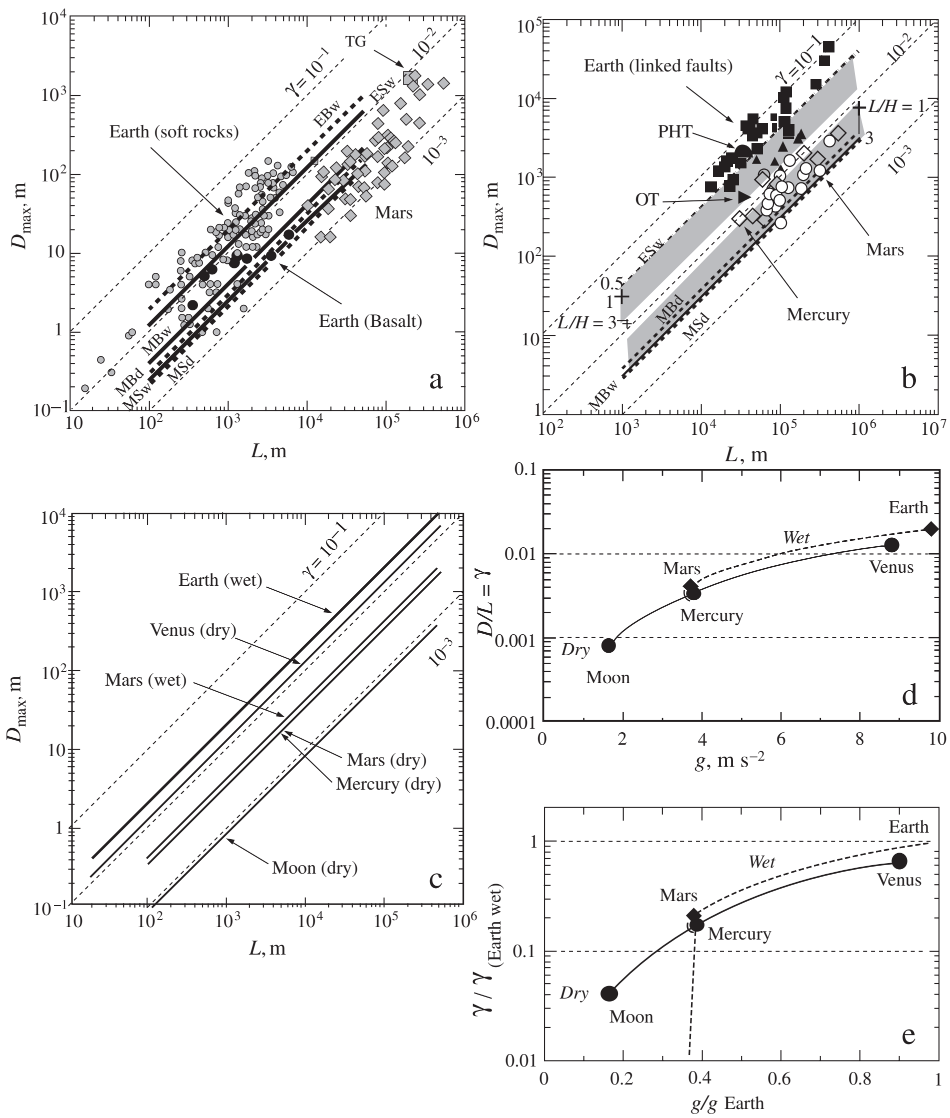

Figure 10.11. Displacement–length scaling relations for planetary faults (after Schultz *et al*., 2006). (a) D_{max}–L data for normal faults from Earth (gray circles, sandstone and non-welded tuff; black circles, basalt) and Mars (gray diamonds, Tempe Terra; gray square, Thaumasia graben, linked faults, 'TG'); data from Schlische *et al*. (1996), Wilkins *et al*. (2002), and Hauber and Kronberg (2005). Calculated scaling relations (see Schultz *et al*., 2006 for parameters): EBw, Earth basaltic rock mass with wet conditions; ESw, Earth sandstone rock mass with wet conditions; MBw, Mars basaltic rock mass with wet conditions; MBd, Mars basaltic rock mass with dry conditions; MSw, Mars sandstone rock mass with wet conditions; MSd, Mars sandstone rock mass with dry conditions. (b) D_{max}–L data for thrust faults from Earth (black squares and triangles), Mars (open circles) and

P1: aaa Trim: 174mm × 247mm Top: 0.553in Gutter: 0.747in
CUUK632-10 CUUK632-Watters ISBN: 978 0 521 76573 2 June 26, 2009 21:33

ice stiffness (e.g., Nimmo and Schenk, 2006) along with reduced surface gravities of those satellites. Lunar faults will likely scale with its smaller surface gravity as well, with faults that cut highland regolith (which has significantly smaller values of modulus than does basalt) exhibiting larger displacements than those that cut mare basalts, all other factors equal (see Watters and Johnson, Chapter 4).

Comparisons of displacement–length scaling between planets and satellites should also be made for faults that do not cut through the mechanical or thermal lithosphere, so that flexure or tilting of faulted blocks does not contribute to increased values of offset (e.g., Cowie and Scholz, 1992b; Nimmo and Schenk, 2006). Additionally, faults should be isolated from other, nearby faults (i.e., not segments from a fault zone or rift) and not be stratigraphically restricted to ensure the clearest comparison with terrestrial and other data that are collected following these guidelines. Because fault-related strains depend on the D_{max}/L ratio along with the fault density (Gupta and Scholz, 2000b; Schultz, 2003a), the average strain accommodated by faulting at the surface of a planetary body, for the same style of tectonic domain, may generally decrease as a function of gravity.

4 Fault-related topography

The topographic signature of a fault at the planetary surface reveals its geometry and characteristics in the subsurface, as demonstrated from many terrestrial studies (e.g., Ma and Kusznir, 1993; Willemse, 1997; Niño *et al*., 1998; Soliva and Benedicto, 2005). For example, the magnitude and distribution of uplift along normal faults (i.e., the small footwall uplift on normal fault or graben flanks; Weissel and Karner, 1989) and thrust faults (i.e., the major uplift on the upper plate called

←

Mercury (gray diamonds); data from Elliott (1976), black squares; Mége and Riedel (2001), black triangles; Shaw *et al*. (2002), black circle (Puente Hills Blind-Thrust System, ‘PHT’); Davis *et al*. (2005), right-pointing black triangle (Ostler Thrust, ‘OT’); Watters *et al*. (2000, 2002); and Watters (2003). Calculated scaling relations labeled as in (a) but with $L/H = 0.5$ for terrestrial thrust faults with lower ticks at $L/H = 1.0$ and 3.0 (upper shaded region in the figure), and $L/H = 3.0$ for Martian and mercurian thrust faults with upper tick at $L/H = 1.0$ (lower shaded region). (c) Predicted values of D_{max}/L for smaller planets and satellites. All curves calculated for normal faults assuming $L/H = 3$, $N = 3000$, and basaltic rock-mass parameters. (d) Summary of D_{max}–L scaling for terrestrial planets calculated for wet basaltic crusts (dashed curves) and dry basaltic crusts (solid curves). (e) D_{max}–L scaling values for smaller planets normalized by (wet) terrestrial ones.

P1: aaa Trim: 174mm × 247mm Top: 0.553in Gutter: 0.747in
CUUK632-10 CUUK632-Watters ISBN: 978 0 521 76573 2 June 26, 2009 21:33

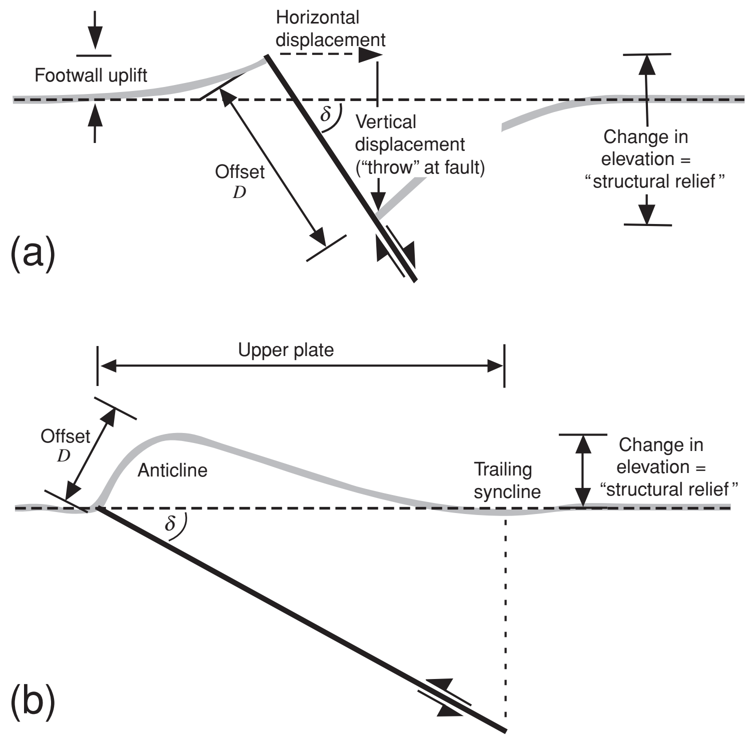

Figure 10.12. Relationships between cumulative fault offset D, fault dip angle δ, and structural topography, shown in crosssection, due to deformation of the planetary surface by the faulting for (a) normal faults (after Schultz and Lin, 2001) and (b) thrust faults (after Schultz, 2000b).

"lobate ridges" on the Moon, Mars, and Mercury, Figure 10.12; Niño *et al*., 1998; Cohen, 1999; Schultz, 2000b; Ma and Kusznir, 2003) is a function of the map length and down-dip height of an individual fault. Topographic uplift across faults is also a reliable indicator of the subsurface fault geometry on Mars (e.g., Schultz, 1999, 2000b; Schultz and Lin, 2001; Schultz and Watters, 2001; Watters *et al*., 2002; Wilkins *et al*., 2002; Wilkins and Schultz, 2003; Okubo and Schultz, 2003, 2004, 2006a; Polit *et al*., 2009), where outstanding high-resolution topographic data currently exist.

Because erosion and degradation of topography is relatively slow on Mars, fault-related topography is well expressed, especially for younger faults. However, even Noachian thrust faults (with ages ∼4 Ga; see Figure 8.1 of Tanaka *et al*., Chapter 8) have topography that is sufficiently well preserved to reveal the subsurface details (e.g., Schultz, 2003b; Okubo and Schultz, 2003, 2004; Goudy *et al*., 2005; Grott *et al*., 2006). For example, forward mechanical models of the topography, both boundary element and finite element, produced by normal faults (Schultz and Lin,

P1: aaa Trim: 174mm × 247mm Top: 0.553in Gutter: 0.747in
CUUK632-10 CUUK632-Watters ISBN: 978 0 521 76573 2 June 26, 2009 21:33

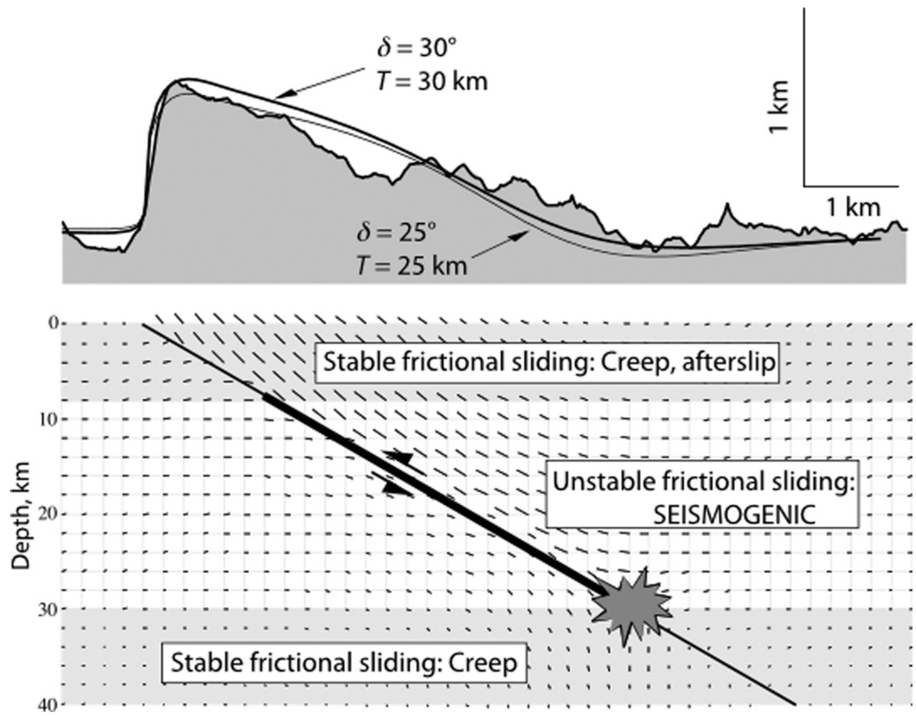

Figure 10.13. Topography measured across Amenthes Rupes, a Martian surface-breaking thrust fault, along with the topography predicted from 1.5 km of slip along the thrust fault (after Schultz and Watters, 2001). Lower panel shows the predicted displacement trajectories in the Martian lithosphere associated with the Amenthes Rupes thrust fault, with the orientation and length of the tick marks indicating the predicted local direction and magnitude of displacements; the largest values occur above the thrust fault (the "upper plate"). Regimes of Martian frictional stability shown as shaded regions and labeled; star indicates maximum depth of seismic rupture along the fault (after Schultz, 2003b).

2001; Hauber and Kronberg, 2005) and thrust faults (Schultz, 2000b; Schultz and Watters, 2001; Watters *et al.*, 2002; Okubo and Schultz, 2004; Grott *et al.*, 2006) demonstrate how topographic profiles across faults on Mars, and also Mercury, can be used to accurately determine the dip angle and depth of faulting (Figure 10.13). These models calculate the displacements on faults subject to a specified set of conditions, including remote tectonic stresses, fault geometry and constitutive relations such as frictional strength, and material properties of the surrounding rock, and then calculate the associated topographic changes of the planetary surface (see Schultz and Aydin, 1990; Schultz, 1992; and Okubo and Schultz, 2004, for details of the boundary element method and appropriate parameters used in the program FAULT to make these calculations). The topographic changes along Martian strike-slip faults (Schultz, 1989; Okubo and Schultz, 2006b) provide an additional avenue

P1: aaa Trim: 174mm × 247mm Top: 0.553in Gutter: 0.747in
CUUK632-10 CUUK632-Watters ISBN: 978 0 521 76573 2 June 26, 2009 21:33

for exploring fault geometry and lithospheric stress states (e.g., Andrews-Hanna *et al*., 2008).

Investigation of MOLA profiles has also revealed evidence of igneous dikes below certain Martian grabens (Schultz *et al*., 2004) by detection of the subtle yet diagnostic topographic signature (e.g., Rubin and Pollard, 1988; Mastin and Pollard, 1988; Rubin, 1992) produced above a dike at the planetary surface (see also Goudy and Schultz, 2005). An example is shown in Figure 10.14. Perhaps counterintuitively at first thought, the rock directly above the dike tip is neither displaced nor extended to any large degree, but instead, the planetary surface on either side of a dike is displaced upward and outward, forming the characteristic pair of gentle topographic swells shown in Figure 10.14c (and noted, for example, by Rubin and Pollard, 1988). In contrast, the surface topography associated with slip along two inward-dipping normal faults is elevated yet concave-upward in the footwall (Rubin and Pollard, 1988; Weissel and Karner, 1989; Schultz and Lin, 2001; see Figure 10.12a) and decays more rapidly with distance away from the fault than does the topographic rise produced by dike inflation (Figure 10.14c). The several distinctive characteristics of the topographic signatures of normal faults and subsurface dikes, apparent in Figures 10.12a and 10.14c, permit the identification of the type of extensional structure beneath a planetary surface (i.e., dike or fault).

The flanking topographic uplifts above a dike also correspond to the locations of increased horizontal tensile stresses, noted previously, for example, by Williams (1957) and Delaney *et al*. (1986) and related to bending of the rock there. Given sufficient bending, ground cracks and two inward-dipping normal faults can nucleate at the topographic crests and propagate downward, forming a structural graben above the dike (e.g., Rubin and Pollard, 1988; Mastin and Pollard, 1988; Rubin, 1992; Schultz, 1996; Figure 10.14b) whose width scales with the depth to the dike top (Rubin and Pollard, 1988; Mastin and Pollard, 1988; Schultz, 1996; Okubo and Martel, 1998; Schultz *et al*., 2004). The predicted displacement trajectories in the Martian lithosphere associated with inflation of the dike (Figure 10.14d) indicate that most of the deformation of a planetary lithosphere occurs closest to the dike, with the magnitude of deformation decreasing away from it, consistent with previous work on terrestrial dike-related topographic changes. The displacement magnitudes in the lithosphere scale with the magma pressure and inversely with lithospheric stiffness (Young's modulus). Assessment of the subsurface structure in areas of planetary volcanotectonic activity is critical to evaluating the relationships, for example, between regional extension, faulting, and dike intrusion (e.g., Grosfils and Head, 1994; Koenig and Pollard, 1998; Ernst *et al*., 2001; Wilson and Head, 2002; Mège *et al*., 2003; Schultz *et al*., 2004) and between groundwater discharge in Martian outflow channels and the associated dike-related grabens (Hanna and Phillips, 2006).

P1: aaa Trim: 174mm × 247mm Top: 0.553in Gutter: 0.747in
CUUK632-10 CUUK632-Watters ISBN: 978 0 521 76573 2 June 26, 2009 21:33

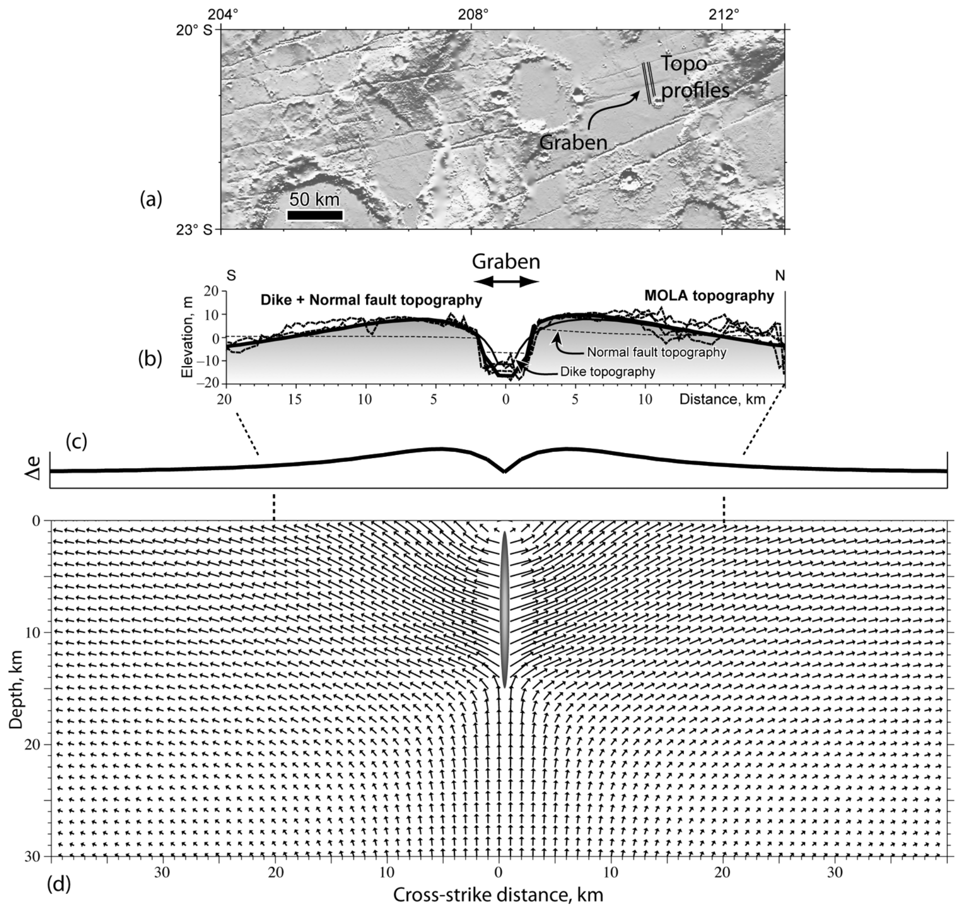

Figure 10.14. Deformation of a planetary surface due to dilation of a subsurface igneous dike, following Schultz *et al*. (2004). (a) Shaded relief image showing several northeast-trending grabens in the Tharsis region of Mars; the locations of four MOLA topographic profiles oriented normal to one of these grabens are indicated. (b) Topographic slice across the graben shown in (a) showing the four MOLA profiles (heavy dashed lines) and three predictions of structural topography: uplift due only to a subsurface dike (smooth curve; parameters given in Schultz *et al*., 2004), uplift due only to the graben-bounding normal faults (fine dashed curve), and the sum of dike and fault topographies (bold curve). The location of the graben at the crest of regional dike-related topography is indicated. (c) Predicted surface topography above a dike. (d) The predicted displacement trajectories in the Martian lithosphere associated with inflation of a dike due to magma pressure, shown following Figure 10.13 but here with arrowheads.

P1: aaa Trim: 174mm × 247mm Top: 0.553in Gutter: 0.747in
CUUK632-10 CUUK632-Watters ISBN: 978 0 521 76573 2 June 26, 2009 21:33

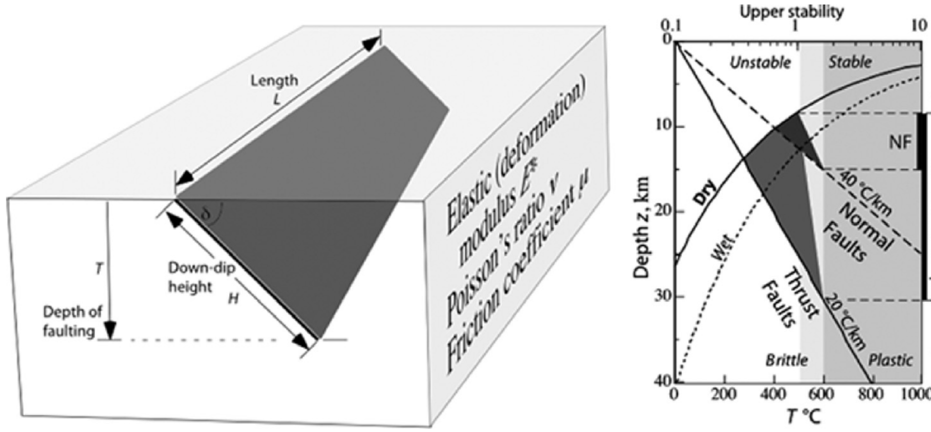

Figure 10.15. The depth of faulting *T* is related to the down-dip height *H* of the coseismic displacement distribution on a planetary fault (left panel, after Schultz and Lin, 2001) and, in turn, to the 600 °C isotherm for mafic rocks (right panel, after Schultz, 2003b), appropriate to most silicate planetary bodies.

The maximum depth of faulting *T* in a planetary lithosphere of mafic composition is defined approximately by the 600 °C isotherm (Abercrombie and Ekström, 2001; Grott *et al*., 2006; Knapmeyer *et al*., 2006), which is associated with the lower stability transition between unstable (seismogenic) frictional sliding above and stable sliding (creep) below (e.g., Tse and Rice, 1986; Scholz, 1998). Using the best-fit value of $T = 30$ km (Schultz and Watters, 2001; Grott *et al*., 2006) for the faulted domain at Amenthes Rupes in Arabia Terra (eastern Mars), the paleogeothermal gradient during Martian thrust faulting was approximately 20 °C km^{-1} (assuming a surface temperature of ∼0 °C and an approximately linear gradient). Down-dip portions of the Martian thrust faults, deeper than 30 km, would tend to slip stably but would contribute only small components to the surface topography, given their greater depth below the surface (e.g., Cohen, 1999). On the other hand, Martian normal faults in Tempe Terra and Alba Patera attain depths of ∼15 km (Wilkins *et al*., 2002; Polit *et al*., 2009), implying a paleogeothermal gradient there of about 40 °C km^{-1} (Figure 10.15).

The upper (shallow) limit of seismogenic slip is related to the upper stability transition (Marone, 1998; Scholz, 1998), above which fault zone material (such as gouge) is velocity strengthening (Marone and Scholz, 1988). This upper stability transition is pressure dependent and independent of fault type (Scholz, 1998). By scaling the values used for terrestrial faults (3–4 km: Cowie *et al*., 1994; Scholz, 1998, and hydrostatic pore-fluid conditions) to Martian conditions ($g = 3.7\ \mathrm{m\,s^{-2}}$), frictional sliding along Martian faults should be conditionally stable (barring large perturbations, such as Marsquakes on subjacent or nearby fault segments, or rapid

P1: aaa Trim: 174mm × 247mm Top: 0.553in Gutter: 0.747in
CUUK632-10 CUUK632-Watters ISBN: 978 0 521 76573 2 June 26, 2009 21:33

healing processes; see Scholz, 1998) at depths shallower than ∼8–10 km for a "wet" lithosphere (hydrostatic pore-fluid pressure) or ∼5–7 km for a "dry" lithosphere. An active hydrologic system ("wet" lithosphere), along with slow slip rates along the faults, would promote healing of the fault zone, leading to decreasing depth for the upper stability transition.

Seismogenic (unstable) frictional sliding along the largest thrust fault in the Amenthes Rupes population (Schultz, 2003b) should have occurred primarily between depths of 8 and 30 km (with the depth of the lower stability transition corresponding to the likely marsquake nucleation depth; Figure 10.15). Using the depth range obtained above for unstable frictional sliding, ∼82% of the total moment release and strain associated with the Martian thrust fault population was seismogenic (assuming $L/H = 3$; 80% for $L/H = 2$). The fraction of seismogenic strain for a given Martian fault population will decrease for smaller and less deeply penetrating surface-breaking faults given that the upper ∼8 km globally should remain largely devoid of nucleating marsquakes along normal, strike-slip, or thrust faults.

5 Strain

The strain signature associated with the three fault types is well known (e.g., Reches, 1978, 1983; Krantz, 1988, 1989), as shown in Figure 10.2. In an extending tectonic domain with coaxial stress–strain relations, the vertical principal stress is the lithostat and the two horizontal principal stresses are smaller in magnitude but still compressive, as shown by *in situ* stress measurements on the Earth (McGarr and Gay, 1978; Brown and Hoek, 1978; Plumb, 1994; Zoback *et al*., 2003). The domain extends in the direction of the least horizontal principal stress and thins vertically, producing an extensional normal strain horizontally and a contractional (thinning) normal strain vertically. For thrust faulting, the maximum principal stress is horizontal and the lithostat becomes the least principal stress (both are, of course, compressive, as is the intermediate (horizontal) principal stress), leading to lithospheric thickening (with an extensional vertical normal strain) and horizontal shortening normal to the maximum (horizontal) principal stress. For strike-slip faulting, the lithostat serves as the intermediate (compressive) principal stress, and the maximum and minimum (compressive) principal stresses are horizontal, leading to a contractional normal strain perpendicular to the maximum horizontal principal stress direction and an extensional normal strain perpendicular to the minimum horizontal principal stress direction. Shear strains can also be calculated for these fault types, as well as the more complicated, spatially varying, inhomogeneous displacement and strain fields that are particularly significant within a few fault lengths of a fault (e.g., Chinnery, 1961; Barnett *et al*., 1987; Ma and Kusznir, 1993).

P1: aaa Trim: 174mm × 247mm Top: 0.553in Gutter: 0.747in
CUUK632-10 CUUK632-Watters ISBN: 978 0 521 76573 2 June 26, 2009 21:33

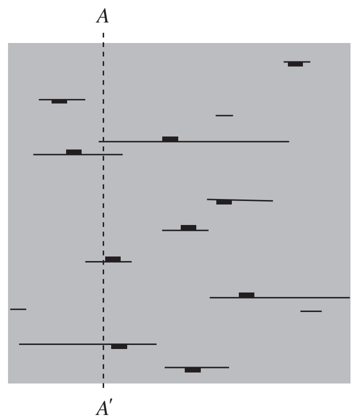

Figure 10.16. A one-dimensional (1-D) sampling traverse (A–A′) across a fault population. This sparse fault population suggests how the value of strain depends on where the traverse is taken.

An extensive literature exists on how the amount of strain accommodated by a population of faults can be quantified (see Kostrov, 1974; Segall, 1984a,b; Wojtal, 1989; Scholz and Cowie, 1990; Marrett and Allmendinger, 1991; Westaway, 1994; Scholz, 1997; and Borgos *et al*., 2000, for representative approaches). Using the approach of a simple horizontal one-dimensional (1-D, line) traverse across a deformed region (e.g., Golombek *et al*., 1996; see Figure 10.16), the amount of displacement across each fault is first measured from topographic data and then corrected to take into account only the component of displacement parallel to the traverse (i.e., correct for strike and dip; Peacock and Sanderson, 1993; Scholz, 1997; see below). For closely spaced faults (called "penetrative deformation") it may be easier to trace the offset of a passive marker from one side to the other, instead of measuring all the fault displacements; see Pappalardo and Collins (2005) for a calculation of the strains along a dense, closely-spaced fault population on Ganymede. However, many planetary fault populations tend to be sparse – that is, faults that are widely spaced relative to their lengths (e.g., Segall, 1984a; Barnett *et al*., 1987). Strains measured along a 1-D traverse can therefore miss many small faults. In addition, measurements of fault offset will likely not be made at the positions of maximum fault displacement for all faults transected by the traverse.

Instead of using a 1-D line traverse for calculating strain, an alternative approach to obtaining fault-related normal strain parallels that from seismology, i.e., relating incremental displacements accumulated along rupture patches during an earthquake and the total (or cumulative) displacements accumulated along faults (e.g., Segall, 1984a; Scholz and Cowie, 1990; Scholz, 1997). Any fault has three characteristic dimensions, including length L (defined as its horizontal dimension), maximum

P1: aaa Trim: 174mm × 247mm Top: 0.553in Gutter: 0.747in
CUUK632-10 CUUK632-Watters ISBN: 978 0 521 76573 2 June 26, 2009 21:33

$D_{\max}$ or average D displacement (usually located near the fault's midpoint), and height H (measured normal to length, along the fault plane, in the vertical or down-dip direction). The procedure for calculating the average horizontal normal strain for a deforming region, for example, is straightforward and examined in this section. Specifically, the three variables (L, D, and H) for each fault in the population are assessed (see Figure 10.10c), summed, and then divided by the dimensions of the deforming region.

First the geometric moment M_g is calculated, which is given by

$$M_g = DLH \tag{10.5}$$

and which is defined by *average* displacement D, fault length L, and down-dip fault height H, with units of m^3 (King, 1978; Scholz and Cowie, 1990; Ben-Zion, 2001). D is the average offset along the fault (not $D_{\max}$), measured in the plane of the fault; it is not the component in a horizontal plane, as will be needed later for the horizontal normal strains for extension or contraction. The geometric moment represents the volume of deformed rock associated with a fault population. As a fault grows in size, its surface area increases; because a fault's displacement scales with L, the geometric moment M_g increases as a fault grows in size and in displacement.

The amount of deformation attributed to each fault is given by a related scalar quantity, the quasi-static fault moment M_f (see Pollard and Segall, 1987, p. 302):

$$M_f = GAD = GM_g = GDLH, \tag{10.6}$$

where G is the shear modulus of the surrounding rock mass (where $G = E/[2(1-\nu^2)]$), A is the surface area of the fault as defined by its shape (length L times height H), and D is the average (relative) displacement across the fault. M_f has units of MJ (joules × 10^6) for values of modulus in 10^6 Pa and L, H, and D in meters. The quasi-static fault moment represents the total energy consumed by the rock mass in producing the fault displacements within the region.

The work done by faulting, as recorded in the measured fault displacements, W_f, is the sum of the quasi-static fault moments for all faults in a region:

$$W_f = \sum_{i=1}^{N} (M_f)_i, \tag{10.7}$$

where M_{fi} is the quasi-static moment for each fault and N is the total number of faults in the region. The work also has units of energy (MJ) or, equivalently, 10^6 N m. W_f does not explicitly depend on the size of the deforming region that contains the faults, and it also neglects the generally much smaller contributions of processes such as fault formation. Although there are some implicit relationships between the quantities in Equations (10.6) and (10.7) and region size (e.g., A may

P1: aaa Trim: 174mm × 247mm Top: 0.553in Gutter: 0.747in
CUUK632-10 CUUK632-Watters ISBN: 978 0 521 76573 2 June 26, 2009 21:33

be limited by stratal or crustal thickness (Scholz and Cowie, 1990; Westaway, 1994; see also Figures 10.10c and 10.13), and D and G may depend on scale and driving stress (Cowie and Scholz, 1992b; Schultz *et al.*, 2006), the total work done by faulting (Equation (10.7)) represents a convenient method for quantifying the role of faulting in lithospheric deformation.

Fault strain is a tensor quantity, with components such as normal and shear strain in various directions. For example, the total strain accommodated by a population of normal faults will have a component of extensional normal strain, perpendicular to the average strike of the faults (their "extension direction"), another component of extensional normal strain parallel to the fault strike (which will be small for most cases; e.g., Krantz, 1988), and a component of contractional normal strain in the vertical direction, corresponding to crustal thinning (e.g., Wilkins *et al.*, 2002). Similarly, a thrust fault population will have a component of contractional normal strain perpendicular to the average strike of the faults (their shortening or "vergence" direction), another component of contractional normal strain parallel to the fault strike, and a component of extensional normal strain in the vertical direction, corresponding to crustal thickening (e.g., Schultz, 2000b).

The desired components of the strain tensor can be obtained by using either of two methods. First, all the information needed for Equation (10.6) – the geometric fault moment – can be specified, along with fault dip, fault strike, and displacement rake for each fault. The component of interest can be obtained by solving Kostrov's (1974) equation

$$\varepsilon_{kl} = \frac{1}{2V}\sum_{i=1}^{N}\left(M_f\right)_i, \tag{10.8}$$

as outlined by Aki and Richards (1980, pp. 117–118) and which as been used extensively in seismotectonics and structural geology (e.g., Molnar, 1983; Scholz and Cowie, 1990; Westaway, 1992; Scholz, 1997; Scholz, 2002, pp. 306–309; see also Wilkins *et al.*, 2002; Schultz, 2003a,b; Knapmeyer *et al.*, 2006; Dimitrova *et al.*, 2006, for applications to planetary fault populations). Alternatively, measurements along a traverse can be taken, corrected explicitly for fault strike and rake, and then substituted into a simpler set of strain equations that already have the dip correction incorporated into them (e.g., Scholz, 1997). This second, simpler method for obtaining the horizontal normal strain perpendicular to the average strike of a set of faults, which is probably the most important and widely used quantity in planetary fault population studies, is outlined next, although both methods will produce the same results.

P1: aaa Trim: 174mm × 247mm Top: 0.553in Gutter: 0.747in
CUUK632-10 CUUK632-Watters ISBN: 978 0 521 76573 2 June 26, 2009 21:33

The strike correction, for normal or thrust faults, is the component of $D_{\max}$ in a particular horizontal direction (e.g., Priest, 1993, pp. 96–97; Peacock and Sanderson, 1993). This is obtained by calculating the component of fault displacement D_s along the direction of interest, such as a traverse line (such as one perpendicular to the average strike of a set of faults), by using

$$D_s = D_{\max} \left|\cos(\Delta\psi)\right| , \tag{10.9}$$

in which $\Delta\psi =$ (strike of fault ψ minus the strike of traverse ψ_{T}). The component of horizontal displacement along the traverse direction is given by

$$D_{s,d} = D_{\max} \left|\cos(\Delta\psi)\right| \cos\delta, \tag{10.10}$$

which includes the dip correction (given by the last term in Equation (10.10)).

The other correction that must be made to the displacement data is to reduce the value of $D_{\max}$ to an average value of displacement for the fault. The average displacement D is used in fault-set inversions for paleostresses (e.g., Marrett and Allmendinger, 1990; Angelier, 1994), as well as for fault-related strain (e.g., Scholz and Cowie, 1990; Scholz, 1997). The average displacement $D = \kappa D_{\max}$, where κ is a fraction of the maximum displacement $D_{\max}$, depending on the specific displacement distribution along the fault. Scholz and Cowie (1990) assumed a value of $\kappa = 0.5$. Dawers *et al*. (1993) obtained values of κ for small normal faults in Bishop Tuff of 0.61; Moore and Schultz (1999) found values of κ between 0.3 and 0.7 for normal faults from Canyonlands National Park. A fault having a linear displacement profile has $\kappa = 0.5$, whereas one with an ideal elliptical profile (assuming LEFM conditions) has $\kappa = 0.7854$.

Using these three corrections to $D_{\max}$, the horizontal normal strain due to a particular fault can be calculated. The horizontal normal strain ε_n is M_g normalized by the appropriate dimension of the faulted region having thickness T, horizontal area A, and volume $V = TA$. For "small" faults (e.g., Scholz and Cowie, 1990; Scholz, 1997) (Figure 10.17), $H_i < T/\sin\delta_i$; for "large" faults, $H_i = T/\sin\delta_i = H_0$, so the horizontal normal strain (assuming constant fault dip angles) is obtained from Kostrov's equation (8) explicitly as (e.g., Scholz, 1997)

$$\begin{aligned} \varepsilon_n &= \frac{\sin 2\delta}{2V} \sum_{i=1}^{N} \left[D_i L_i H_i\right] \\ \varepsilon_n &= \frac{\sin 2\delta}{2AT} \sum_{i=1}^{N} \left[D_i L_i \frac{T}{\sin\delta}\right]. \end{aligned} \tag{10.11}$$

The first of Equation (10.11) is for small faults, the second is the approximate limiting value for large faults. "Large" faults in a population, as discussed in this section, are considered to be vertically restricted; "small" faults in a population

P1: aaa Trim: 174mm × 247mm Top: 0.553in Gutter: 0.747in
CUUK632-10 CUUK632-Watters ISBN: 978 0 521 76573 2 June 26, 2009 21:33

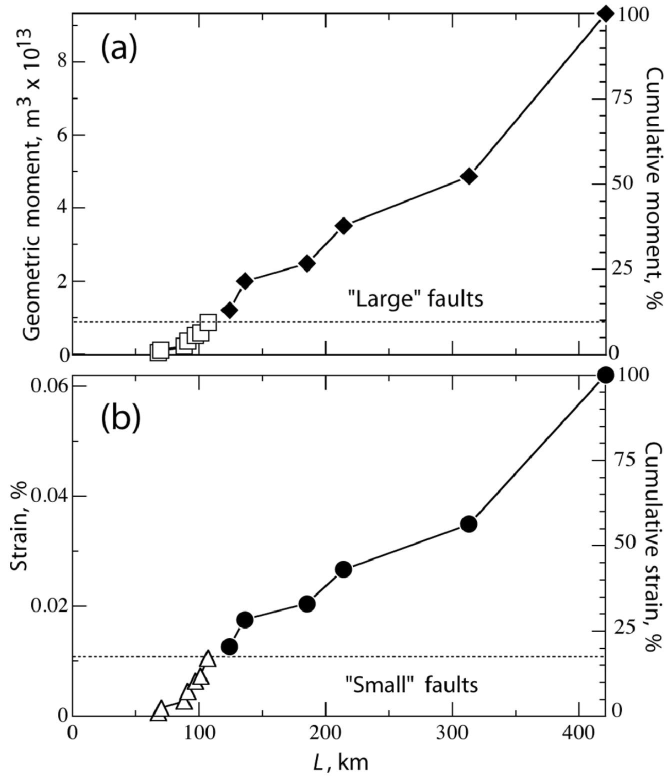

Figure 10.17. (a) Geometric moment and (b) contractional horizontal normal strain (shown as absolute values) calculated for thrust faults within the Amenthes Rupes population of eastern Mars (after Schultz, 2003b).

are unrestricted (Figure 10.10c). Using the trigonometric substitution $\sin 2\delta = 2\sin\delta\cos\delta$ and collecting terms, the horizontal normal strain is written as

$$\begin{aligned} \varepsilon_n &= \frac{\sin\delta\cos\delta}{V}\sum_{i=1}^{N}[D_i L_i H_i] \\ \varepsilon_n &= \frac{\cos\delta}{A}\sum_{i=1}^{N}[D_i L_i], \end{aligned} \tag{10.12}$$

in which δ is fault dip angle and D is the average displacement on a particular fault (using Equation (10.8) and the correction for average displacement from $D_{\max}$); again, the first of Equation (10.12) is for small faults, the second is for large faults. The sign of D must be specified for these equations, using $D > 0$ for normal faults and $D < 0$ for thrust faults. Using this convention, extensional normal strain will be positive and contractional normal will be negative.

In these equations, M_f is calculated for the component of the complete moment tensor for the population in the horizontal plane (i.e., the planetary surface) and

P1: aaa Trim: 174mm × 247mm Top: 0.553in Gutter: 0.747in
CUUK632-10 CUUK632-Watters ISBN: 978 0 521 76573 2 June 26, 2009 21:33

normal to fault strike (e.g., Aki and Richards, 1980, pp. 117–118; Scholz, 1997). These equations are thus defined for normal or thrust faults, with rakes of 90°, and provide the horizontal normal strain (extension for normal faults, contraction for thrust faults) accommodated by the fault population perpendicular to its strike and in the horizontal plane. Analogous equations can be defined for the shear strain accommodated in the horizontal plane by a population of strike-slip faults, although this fault type is comparatively rare on planetary surfaces except for Earth and Europa.

The **vertical normal strain** associated with dip-slip faulting is given by (Aki and Richards, 1980, pp. 117–118)

$$\begin{aligned} \varepsilon_v &= -\frac{\sin\delta\cos\delta}{V}\sum_{i=1}^{N}[D_i L_i H_i] \\ \varepsilon_v &= -\frac{\cos\delta}{A}\sum_{i=1}^{N}[D_i L_i] \end{aligned} \tag{10.13}$$

(the first expression of Equation (10.13) is again for small faults, the second is the approximate limiting value for large faults). Note the sign change relative to the horizontal fault-normal strain: this is the "odd axis" strain of Krantz (1988, 1989; see Figure 10.2). For normal faulting, this strain component quantifies the amount of lithospheric **thinning**, whereas for thrust faulting, the amount of **thickening** of the faulted section.

Direct calculation of the horizontal normal strain due to dip-slip faulting in any dataset by using Equation (10.12) provides a straightforward measure of the extensional or contractional strain associated by a tectonic event. Similarly, the vertical normal strain (thinning or thickening) of a faulted section can be obtained easily from the same set of measurements. As an example, the moments and contractional horizontal normal strain for the Amenthes Rupes thrust fault population in eastern Mars were calculated from the MOLA topography (Figure 10.15; Schultz, 2003b; Grott *et al.*, 2006). The figure reveals the incremental increases in both quantities due to each fault, as well as the dominant effect of the largest faults in the population.

6 Challenges and future work

Future advances in the study of planetary fault populations can be made through a number of techniques, including the use of high-resolution topography. Digital elevation models (DEMs) derived from stereo observations, and to some extent photoclinometry, have the potential to reveal a wealth of information on the geometry and slip distributions of faults. DEMs with postings of one to tens of meters spacing can be constructed from Mars from imagery acquired by the Mars Orbiter Camera, High Resolution Stereo Camera, Context imager and High Resolution Imaging

P1: aaa Trim: 174mm × 247mm Top: 0.553in Gutter: 0.747in
CUUK632-10 CUUK632-Watters ISBN: 978 0 521 76573 2 June 26, 2009 21:33

Science Experiment (HiRISE) camera (Kirk *et al*., 2003; Neukum *et al*., 2004; Williams *et al*., 2004; Jaumann *et al*., 2005; Kronberg *et al*., 2007). While the public availability of preprocessed DEMs is currently limited, the stereo image data are widely available through NASA's Planetary Data System (http://pds.jpl.nasa.gov) and processing of these image data into DEMs can be achieved with standard software (Albertz *et al*., 2005; Kirk *et al*., 2007).

The potential insight that can be gained from high-resolution DEMs of fault population is well worth the effort of processing these data. Although much work has been accomplished from study of fault-related topography measured by photoclinometry, radar, and MOLA data, analysis of DEMs based on more recent datasets will help to extend the current state of knowledge. Significantly, high-resolution DEMs can help to quantify the geometries and slip distributions of planetary faults that are as short as a few kilometers in length (e.g., Okubo *et al*., 2008b; Polit *et al*., 2009), and help to extend current understanding of populations of faults at comparable length scales (e.g., Figure 10.10b). High-resolution DEMs can also help to resolve key spatial details (such as fault-tip displacements and cross-cutting relationships) of the longer faults that have been previously examined in lower resolution planetary datasets. Images having high spatial resolution from HiRISE, for example, are themselves useful for planetary tectonic studies as they are revealing, for the first time, joints (Okubo and McEwen, 2007) and deformation bands (Okubo *et al*., 2008a) on Mars.

Quantification of the geometries and displacements of planetary fault populations can reveal significant insight into the evolution of planetary surfaces. Measurements of fault-plane dip angles reveal effective fault frictional strengths (Equation (10.2)), providing a means of inferring crustal properties. Further, the sense of fault displacement provides insight into the causative stress state (Figure 10.2). Together, fault dip angle and displacement characteristics can provide important constraints, such as crustal strength and magnitudes of stress and strain in 3-D, for the time span over which a particular fault population was active. In this way, analyses of planetary fault populations of different spatial and temporal distributions will be an important source of boundary conditions for geodynamic models of lithospheric evolution (Grott and Breuer, 2008), as well as interpretations of the geologic history of planetary surfaces.

Acknowledgements

Reviews by Steve Wojtal and Ken Tanaka improved the clarity and flow of the chapter. RAS was supported by grants from NASA's Planetary Geology and Geophysics Program and NASA's Mars Data Analysis Program. DM was supported by grants from CNRS/INSU's Programme National de Planétologie.

P1: aaa Trim: 174mm × 247mm Top: 0.553in Gutter: 0.747in
CUUK632-10 CUUK632-Watters ISBN: 978 0 521 76573 2 June 26, 2009 21:33

References

Abercrombie, R. W. and Ekström, G. (2001). Earthquake slip on oceanic transform faults. *Nature*, **410**, 74–76.

Ackermann, R. V., Schlische, R. W., and Withjack, M. O. (2001). The geometric and statistical evolution of normal fault systems: An experimental study of the effects of mechanical layer thickness on scaling laws. *J. Struct. Geol.*, **23**, 1803–1819.

Aki, K. and Richards, P. G. (1980). *Quantitative Seismology: Theory and Methods*. Vol. I. San Francisco: W. H. Freeman.

Albertz, J., Dorninger, P., Dorrer, E., Ebner, H., Gehrke, S., Giese, B., Gwinner, K., Heipke, C., Howington-Kraus, E., Kirk, R. L., Lehmann, H., Mayer, H., Muller, J.-P., Oberst, J., Ostrovskiy, A., Renter, J., Reznik, S., Schmidt, R., Scholten, F., Spiegel, M., Stilla, U., Wählisch, M., Neukum G., Attwenger, M., Barrett, J., and Casley, S. (2005). HRSC on Mars Express: Photogrammetric and cartographic research. *Photogramm. Eng. Remote Sens.*, **71**, 1153–1166.

Anderson, E. M. (1951). *The Dynamics of Faulting and Dyke Formation, with Applications to Britain*. Edinburgh, Oliver & Boyd.

Andrews-Hanna, J. C., Zuber, M. T., and Hauck II, S. A. (2008). Strike-slip faults on Mars: Observations and implications for global tectonics and geodynamics. *J. Geophys. Res.*, **113**, E08002, doi:10.1029/2007JE002980.

Angelier, J. (1994). Fault slip analysis and paleostress reconstruction. In *Continental Deformation*, ed. P. L. Hancock. New York, Pergamon, pp. 53–100.

Aydin, A. (1988). Discontinuities along thrust faults and the cleavage duplexes. In *Geometries and Mechanisms of Thrusting, with Special Reference to the Appalachians*, ed. G. Mitra and S. Wojtal. *Geol. Soc. Am. Spec. Pap.*, **222**, pp. 223–232.

Aydin, A. (2006). Failure modes of the lineaments on Jupiter's moon, Europa: Implications for the origin of its icy crust. *J. Struct. Geol.*, **28**, 2222–2236.

Aydin, A. and DeGraff, J. M. (1988). Evolution of polygonal fracture patterns in lava flows. *Science*, **239**, 471–476.

Aydin, A. and Nur, A. (1982). Evolution of pull-apart basins and their scale independence. *Tectonics*, **1**, 11–21.

Aydin, A. and Reches, Z. (1982). Number and orientation of fault sets in the field and in experiments. *Geology*, **10**, 107–112.

Aydin, A. and Schultz, R. A. (1990). Effect of mechanical interaction on the development of strike-slip faults with echelon patterns. *J. Struct. Geol.*, **12**, 123–129.

Aydin, A., Schultz, R. A., and Campagna, D. (1990). Fault-normal dilation in pull-apart basins: Implications for the relationship between strike-slip faults and volcanic activity. *Ann. Tectoni.*, **4**, 45–52.

Aydin, A., Borja, R. I., and Eichhubl, P. (2006). Geological and mathematical framework for failure modes in granular rock. *J. Struct. Geol.*, **28**, 83–98.

Bai, T. and Pollard, D. D. (2000). Fracture spacing in layered rocks: A new explanation based on the stress transition. *J. Struct. Geol.*, **22**, 43–57.

Banerdt, W. B., Golombek, M. P., and Tanaka, K. L. (1992). Stress and tectonics on Mars. In *Mars*, ed. H. H. Kieffer, B. M. Jakosky, C. W. Snyder and M. S. Matthews. Tucson AZ: University of Ariz. Press, pp. 249–297.

Barnett, J. A. M., Mortimer, J., Rippon, J. H., Walsh, J. J., and Watterson, J. (1987). Displacement geometry in the volume containing a single normal fault. *Am. Assoc. Petrol. Geol. Bull.*, **71**, 925–937.

P1: aaa Trim: 174mm × 247mm Top: 0.553in Gutter: 0.747in
CUUK632-10 CUUK632-Watters ISBN: 978 0 521 76573 2 June 26, 2009 21:33

Bellahsen, N., Daniel, J.-M., Bollinger, L., and Burov, E. (2003). Influence of viscous layers on growth of normal faults: Insights from experimental and numerical models. *J. Struct. Geol.*, **25**, 1471–1485.

Benedicto, A., Schultz, R., and Soliva, R. (2003). Layer thickness and the shape of faults. *Geophys. Res. Lett.*, **30**, 2076, 10.1029/2003GL018237.

Ben-Zion, Y. (2001). On quantification of the earthquake source. *Seismol. Res. Lett.*, **72**, 151–152.

Bieniawski, Z. T. (1989). *Engineering Rock Mass Classifications: A Complete Manual for Engineers and Geologists in Mining, Civil, and Petroleum Engineering*. New York, Wiley.

Bohnenstiehl, D. R. and Carbotte, S. M. (2001). Faulting patterns near 19°30′S on the East Pacific Rise: Fault formation and growth at a superfast spreading center. *Geochem., Geophys., Geosyst.*, **2**, Paper number 2001GC000156.

Bohnenstiehl, D. R. and Kleinrock M. C. (1999). Faulting and fault scaling on the median valley floor of the Trans-Atlantic Geotraverse (TAG) segment, 26°N on the Mid-Atlantic Ridge. *J. Geophys. Res.*, **104**, 29 351–29 364.

Borgos, H. G., Cowie, P. A., and Dawers, N. H. (2000). Practicalities of extrapolating one-dimensional fault and fracture size-frequency distributions to higher-dimensional samples. *J. Geophys. Res.*, **105**, 28 377–28 391.

Brace, W. F. and Kohlstedt, D. L. (1980). Limits on lithospheric stress imposed by laboratory experiments. *J. Geophys. Res.*, **85**, 6248–6252.

Brady, B. H. G. and Brown, E. T. (1993). *Rock Mechanics for Underground Mining*. London, Chapman and Hall.

Brown, E. T. and Hoek, E. (1978). Trends in relationships between measured in-situ stresses and depth. *Int. J. Rock Mech. Min. Sci. Geomech. Abs.*, **15**, 211–215.

Bürgmann, R., Pollard, D. D., and Martel, S. J. (1994). Slip distributions on faults: Effects of stress gradients, inelastic deformation, heterogeneous host-rock stiffness, and fault interaction. *J. Struct. Geol.*, **16**, 1675–1690.

Caine, J. S., Evans, J. P., and Forster, C. B. (1996). Fault zone architecture and permeability structure. *Geology*, **24**, 1025–1028.

Carbotte, S. M. and Macdonald, K. C. (1994). Comparison of seafloor tectonic fabric at intermediate, fast, and super fast spreading ridges: Influence of spreading rate, plate motions, and ridge segmentation on fault patterns. *J. Geophys. Res.*, **99**, 13 609–13 631.

Chinnery, M. A. (1961). The deformation of the ground around surface faults. *Seismol. Soc. Am. Bull.*, **51**, 355–372.

Cladouhos, T. T. and Marrett, R. (1996). Are fault growth and linkage models consistent with power-law distributions of fault lengths? *J. Struct. Geol.*, **16**, 281–293.

Clark, R. M. and Cox, S. J. D. (1996). A modern regression approach to determining fault displacement-length relationships. *J. Struct. Geol.*, **18**, 147–152.

Cohen, S. C. (1999). Numerical models of crustal deformation in seismic fault zones. *Adv. Geophys.*, **41**, 133–231.

Cooke, M. L. (1997). Fracture localization along faults with spatially varying friction. *J. Geophys. Res.*, **102**, 22 425–22 434.

Cowie, P. A. (1998). Normal fault growth in three dimensions in continental and oceanic crust. In *Faulting and Magmatism at Mid-Ocean Ridges*, ed. R. Buck, P. Delaney, J. Karson and Y. Lagabrielle. AGU Monograph 106, pp. 325–348.

Cowie, P. A. and Roberts, G. P. (2001). Constraining slip rates and spacing for active normal faults. *J. Struct. Geol.*, **23**, 1901–1915.

P1: aaa Trim: 174mm × 247mm Top: 0.553in Gutter: 0.747in
CUUK632-10 CUUK632-Watters ISBN: 978 0 521 76573 2 June 26, 2009 21:33

Cowie, P. A. and Scholz, C. H. (1992a). Displacement-length scaling relationships for faults: Data synthesis and discussion. *J. Struct. Geol.*, **14**, 1149–1156.

Cowie, P. A. and Scholz, C. H. (1992b). Physical explanation for the displacement-length relationship of faults using a post-yield fracture mechanics model. *J. Struct. Geol.*, **14**, 1133–1148.

Cowie, P. A., Malinverno, A., Ryan, W. B. F., and Edwards, M. H. (1994). Quantitative fault studies on the East Pacific Rise: A comparison of sonar imaging techniques. *J. Geophys. Res.*, **99**, 15 205–15 218.

Cowie, P. A., Sornette, D., and Vanneste, C. (1995). Multifractal scaling properties of a growing fault population. *Geophys. J. Inter.*, **122**, 457–469.

Cowie, P. A., Knipe, R. J., and Main, I. G. (1996). Introduction to the Special Issue. *J. Struct. Geol.*, **28** (2/3), v–xi.

Crider, J. G. and Peacock, D. C. P. (2004). Initiation of brittle faults in the upper crust: A review of field observations. *J. Struct. Geol.*, **26**, 691–707.

Crider, J. G. and Pollard, D. D. (1998). Fault linkage: Three-dimensional mechanical interaction between echelon normal faults. *J. Geophys. Res.*, **103**, 24 373–24 391.

Davis, K., Burbank, D. W., Fisher, D., Wallace, S., and Nobes, D. (2005). Thrust-fault growth and segment linkage in the active Ostler fault zone, New Zealand. *J. Struct. Geol.*, **27**, 1528–1546.

Davison, I. (1994). Linked fault systems: Extensional, strike-slip and contractional. In *Continental Deformation*, ed. P. L. Hancock. New York, Pergamon, pp. 121–142.

Dawers, N. H. and Anders, M. H. (1995). Displacement-length scaling and fault linkage. *J. Struct. Geol.*, **17**, 607–614.

Dawers, N. H., Anders, M. H., and Scholz, C. H. (1993). Growth of normal faults: Displacement-length scaling. *Geology*, **21**, 1107–1110.

Delaney, P. T., Pollard, D. D., Ziony, J. I., and McKee, E. H. (1986). Field relations between dikes and joints: Emplacement processes and paleostress analysis. *J. Geophys. Res.*, **91**, 4920–4938.

dePolo, C. M. (1998). A reconnaissance technique for estimating the slip rates of normal-slip faults in the Great Basin, and application to faults in Nevada, USA. Ph.D. thesis, University of Nevada, Reno.

Dimitrova, L. L., Holt, W. E., Haines, A. J., and Schultz, R. A. (2006). Towards understanding the history and mechanisms of Martian faulting: The contribution of gravitational potential energy. *Geophys. Res. Lett.*, **33**, L08202, 10.1029/2005GL025307.

Elliott, D. (1976). The energy balance and deformation mechanism of thrust sheets. *Philos. Trans. R. Soc. Lond.*, **A283**, 289–312.

Engelder, T. (1993). *Stress Regimes in the Lithosphere*. Princeton, NJ, Princeton University Press.

Ernst, R. E., Grosfils, E. B., and Mège, D. (2001). Giant dike swarms: Earth, Venus, and Mars. *Annu. Rev. Earth Planet. Sci.*, **29**, 489–534.

Ferrill, D. A. and Morris, A. P. (2003). Dilational normal faults. *J. Struct. Geol.*, **25**, 183–196.

Fossen, H. and Gabrielsen, R. H. (2005). *Strukturgeologi*. Bergen, Norway, Fagbokforlaget.

Fossen, H., Schultz, R. A., Shipton, Z. K., and Mair, K. (2007). Deformation bands in sandstone: A review. *J. Geol. Soc. Lond.*, **164**, 755–769.

Franklin, J. A. (1993). Empirical design and rock mass characterization. In *Comprehensive Rock Engineering*, ed. J. A. Hudson. Vol. 2, ed. C. Fairhurst. New York. Pergamon Press, pp. 795–806.

P1: aaa Trim: 174mm × 247mm Top: 0.553in Gutter: 0.747in
CUUK632-10 CUUK632-Watters ISBN: 978 0 521 76573 2 June 26, 2009 21:33

Freed, A. M., Melosh, H. J., and Solomon, S. C. (2001). Tectonics of mascon loading: Resolution of the strike-slip faulting paradox. *J. Geophys. Res.*, **106**, 20 603–20 620.

Gawthorpe, R. L. and Hurst, J. M. (1993). Transfer zone in extensional basins: Their structural style and influence on drainage development and stratigraphy. *J. Geol. Soc. Lond.*, **150**, 1137–1152.

Garel, E., Dautiel, O., and Lagabrielle Y. (2002). Deformation processes at fast to ultra-fast oceanic spreading axes: Mechanical approach. *Tectonophy.*, **346**, 223–246.

Goetze, C. and Evans, B. (1979). Stress and temperature in the bending lithosphere as constrained by experimental rock mechanics. *Geophys. J. R. Astron. Soc.*, **59**, 463–478.

Golombek, M. P., Tanaka, K. L., and Franklin, B. J. (1996). Extension across Tempe Terra, Mars, from measurements of fault scarp widths and deformed craters. *J. Geophys. Res.*, **99**, 23 163–23 171.

Goudy, C. L. and Schultz, R. A. (2005). Dike intrusions beneath grabens south of Arsia Mons, Mars. *Geophys. Res. Lett.*, **32**, 5, 10.1029/2004GL021977.

Goudy, C. L., Schultz, R. A., and Gregg, T. K. P. (2005). Coulomb stress changes in Hesperia Planum, Mars, reveal regional thrust fault reactivation. *J. Geophys. Res.*, **110**, E10005, 10.1029/2004JE002293.

Grosfils, E. and Head, J. W. (1994). Emplacement of a radiating dike swarm in western Vinmara Planitia, Venus: Interpretation of the regional stress field orientation and subsurface magmatic configuration. *Earth, Moon and Planets*, **66**, 153–171.

Grott, M. and Breuer, D. (2008). The evolution of the Martian elastic lithosphere and implications for crustal and mantle rheology. *Icarus*, **193**, 503–515.

Grott, M., Hauber, E., Werner, S. C., Kronberg, P., and Neukum, G. (2006). Mechanical modeling of thrust faults in the Thaumasia region, Mars, and implications for the Noachian heat flux. *Icarus*, **186**, 517–526.

Gudmundsson, A. (1992). Formation and growth of normal faults at the divergent plate boundary in Iceland. *Terra Nova*, **4**, 464–471.

Gudmundsson, A. (2004). Effects of Young's modulus on fault displacement. *Comptes Rendus Geosci.*, **336**, 85–92.

Gudmundsson, A. and Bäckström, K. (1991). Structure and development of the Sveeinagja graben, Northeast Iceland. *Tectonophys.*, **200**, 111–125.

Gupta, A. and Scholz, C. H. (2000a). A model of normal fault interaction based on observations and theory. *J. Struct. Geol.*, **22**, 865–879.

Gupta, A. and Scholz, C. H. (2000b). Brittle strain regime transition in the Afar depression: Implications for fault growth and seafloor spreading. *Geology*, **28**, 1078–1090.

Hanna, J. C. and Phillips, R. J. (2006). Tectonic pressurization of aquifers in the formation of Mangala and Athabasca Valles, Mars. *J. Geophys. Res.*, **111**, E03003, doi: 10.1029/2005JE002546.

Harris, R. A. (1998). Introduction to special section: stress triggers, stress shadows, and implications. *J. Geophys. Res.*, **103**, 24 347–24 358.

Hatheway, A. W. and Kiersch, G. A. (1989). Engineering properties of rock. In *Practical Handbook of Physical Properties of Rocks and Minerals*, ed. R. S. Carmichael, Boca Raton, Fl: CRC Press, pp. 672–715.

Hauber, E. and Kronberg, P. (2005). The large Thaumasia graben on Mars: Is it a rift? *J. Geophys. Res.*, **110**, E07003, 10.1029/2005JE002407.

Hoek, E. (1983). Strength of jointed rock masses. *Géotechnique*, **33**, 187–223.

Hoek, E. (1990). Estimating Mohr-Coulomb friction and cohesion from the Hoek-Brown failure criterion. *Int. J. Rock Mech. Min. Sci. Geomech. Abs.*, **27**, 227–229.

P1: aaa Trim: 174mm × 247mm Top: 0.553in Gutter: 0.747in
CUUK632-10 CUUK632-Watters ISBN: 978 0 521 76573 2 June 26, 2009 21:33

Hoek, E. and Brown, E. T. (1980). Empirical strength criterion for rock masses. *J. Geotech. Eng. Div. Am. Soc. Civ. Eng.*, **106**, 1013–1035.

Hoek, E. and Brown, E. T. (1997). Practical estimates of rock mass strength. *Int. J. Rock Mech. Min. Sci.*, **34**, 1165–1186,

Hooper, D. M., Bursik, M. I., and Webb, F. H. (2003). Application of high-resolution, interferometric DEMs to geomorphic studies of fault scarps, Fish Lake Valley, Nevada, California, USA. *Remote Sens. Environ.*, **84**, 255–267.

Hu, M. S. and Evans, A. G. (1989). The cracking and decohesion of thin films on ductile substrate. *Acta Mater.*, **37**, 917–925.

Hubbert, M. K. and Rubey, W. W. (1959). Role of fluid pressure in mechanics of overthrust faulting: I. Mechanics of fluid-filled porous solids and its application to overthrust faulting. *Geol. Soc. Am. Bull.*, **70**, 115–166.

Jaeger, J. C. and Cook, N. G. W. (1979). *Fundamentals of Rock Mechanics*. 3rd edn. New York, Chapman and Hall.

Jaeger, J. C., Cook, N. G. W., and Zimmerman, R. W. (2007). *Fundamentals of Rock Mechanics*. 4th edn. Oxford, Blackwell.

Jaumann, R., Reiss, D., Frei, S., Neukum, G., Scholten, F., Gwinner, K., Roatsch, T., Matz, K.-D., Mertens, V., Hauber, E., Hoffmann, H., Köhler, U., Head, J. W., Hiesinger, H., and Carr, M. H. (2005). Interior channels in Martian valleys: Constraints on fluvial erosion by measurements of the Mars Express High Resolution Stereo Camera. *Geophys. Res. Lett.*, **32**, L16203, 10.1029/2005GL023415.

Kakimi, T. (1980). Magnitude-frequency relation for displacement of minor faults and its significance in crustal deformation. *Bull. Geol. Surv. Jap.*, **31**, 467–487.

Kattenhorn, S. A. and Marshall, S. T. (2006). Fault-induced perturbed stress fields and associated tensile and compressive deformation at fault tips in the ice shell of Europa: Implications for fault mechanics. *J. Struct. Geol.*, **28**, 2204–2221.

Kattenhorn, S. A. and Pollard, D. D. (1999). Is lithostatic loading important for the slip behavior and evolution of normal faults in the Earth's crust? *J. Geophys. Res.*, **104**, 28 879–28 898.

Kattenhorn, S. A. and Pollard, D. D. (2001). Integrating 3D seismic data, field analogs and mechanical models in the analysis of segmented normal faults in the Wytch Farm oil field, southern England. *Am. Assoc. Petrol. Geol. Bull.*, **85**, 1183–1210.

Kiefer, W. S. and Swafford, L. C. (2006). Topographic analysis of Devana Chasma, Venus: Implications for rift system segmentation and propagation. *J. Struct. Geol.*, **28**, 2144–2155.

King, G. C. P. (1978). Geological faulting: Fracture, creep and strain. *Philos. Trans. R. Soc. Lond.*, **A288**, 197–212.

King, G. and Yielding, G. (1984). The evolution of a thrust fault system: Processes of rupture initiation, propagation and termination in the 1980 El Asnam (Algeria) earthquake. *Geophys. J. R. Astron. Soc.*, **77**, 915–933.

King, G. C. P., Stein, R. S., and Lin, J. (1994). Static stress changes and the triggering of earthquakes. *Seismol. Soc. Am. Bull.*, **84**, 935–953.

Kirk, R. L., Howington-Kraus, E., Redding, B., Galuszka, D., Hare, T. M., Archinal, B. A., Soderblom, L. A., and Barrett, J. M. (2003). High-resolution topomapping of candidate MER landing sites with Mars Orbiter Camera narrow-angle images. *J. Geophy. Res.*, **108**, 8088, 10.1029/2003JE002131.

Kirk R. L., Howington-Kraus, E., Rosiek, M. R., Cook, D., Anderson, J., Becker, K., Archinal, B. A., Keszthelyi, L., King, R., McEwen, A. S., and the HiRISE Team (2007). Ultrahigh resolution topographic mapping of Mars with HiRISE stereo

P1: aaa Trim: 174mm × 247mm Top: 0.553in Gutter: 0.747in
CUUK632-10 CUUK632-Watters ISBN: 978 0 521 76573 2 June 26, 2009 21:33

images: Methods and first results. *Seventh International Conference on Mars*, abstract 3381.

Knapmeyer, M., Oberst, J., Hauber, E., Wählisch, M., Deuchler, C., and Wagner, R. (2006). Working models for spatial distribution and level of Mars' seismicity. *J. Geophys. Res.*, **111**, E11006, 10.1029/2006JE002708.

Koenig, E. and Aydin, A. (1998). Evidence for large-scale strike-slip faulting on Venus. *Geology*, **26**, 551–554.

Koenig, E. and Pollard, D. D. (1998). Mapping and modeling of radial fracture patterns on Venus. *J. Geophys. Res.*, **103**, 15 183–15 202.

Kohlstedt, D. L., Evans, B., and Mackwell, S. J. (1995). Strength of the lithosphere: constraints imposed by laboratory experiments. *J. Geophys. Res.*, **100**, 17 587–17 602.

Kostrov, B. (1974). Seismic moment and energy of earthquakes, and seismic flow of rock. *Izvestiya*, *Phys. Solid Earth*, **13**, 13–21.

Krantz, R. W. (1988). Multiple fault sets and three-dimensional strain: Theory and application. *J. Struct. Geol.*, **10**, 225–237.

Krantz, R. W. (1989). Orthorhombic fault patterns: The odd axis model and slip vector orientations. *Tectonics*, **8**, 483–495.

Kronberg, P., Hauber, E., Grott, M., Werner, S. C., Schäfer, T., Gwinner, K., Giese, B., Masson, P., and Neukum, G. (2007). Acheron Fossae, Mars: Tectonic rifting, volcanism, and implications for lithospheric thickness. *J. Geophys. Res.*, **112**, E04005, 10.1029/2006JE002780.

Lucchitta, B. K. (1976). Mare ridges and related highland scarps: Results of vertical tectonism? *Proc. Lunar Sci. Conf.*, **7**, 2761–2782.

Ma, X. Q. and Kusznir, N. J. (2003). Modelling of near-field subsurface displacements for generalized faults and fault arrays. *J. Struct. Geol.*, **15**, 1471–1484.

Mangold, N., Allemand, P., and Thomas, P. G. (1998). Wrinkle ridges of Mars: Structural analysis and evidence for shallow deformation controlled by ice-rich décollements. *Planet. Space Sci.*, **46**, 345–356.

Manighetti, I., King, G. C. P., Gaudemer, Y., Scholz, C. H., and Doubre, C. (2001). Slip accumulation and lateral propagation of active normal faults in Afar. *J. Geophys. Res.*, **106**, 13 667–13 696.

Manighetti I., Campillo, M., Sammis, C., Mai, P. M., and King, G. (2005). Evidence for self-similar, triangular slip distributions on earthquakes: Implications for earthquake and fault mechanics. *J. Geophys. Res.*, **110**, B05302, doi:10.1029/2004JB003174.

Mansfield, C. S. and Cartwright, J. A. (1996). High resolution fault displacement mapping from three-dimensional seismic data: Evidence for dip linkage during fault growth. *J. Struct. Geol.*, **18**, 249–263.

Marone, C. (1998). Laboratory-derived friction laws and their application to seismic faulting. *Annu. Rev. Earth Planet. Sci.*, **26**, 643–696.

Marone, C. and Scholz, C. H. (1988). The depth of seismic faulting and the transition from stable to instable slip regimes. *Geophys. Res. Lett.*, **15**, 621–624.

Marrett, R. and Allmendinger, R. W. (1990). Kinematic analysis of fault slip data. *J. Struct. Geol.*, **12**, 973–986.

Marrett, R. and Allmendinger, R. W. (1991). Estimates of strain due to brittle faulting: Sampling of fault populations. *J. Struct. Geol.*, **13**, 735–738.

Marrett, R., Orteg, O. J., and Kelsey, J. M. (1999). Extent of power-law scaling for natural fractures in rocks. *Geology*, **27**, 799–802.

Martel, S. J. (1997). Effects of cohesive zones on small faults and implications for secondary fracturing and fault trace geometry. *J. Struct. Geol.*, **19**, 835–847.

P1: aaa Trim: 174mm × 247mm Top: 0.553in Gutter: 0.747in
CUUK632-10 CUUK632-Watters ISBN: 978 0 521 76573 2 June 26, 2009 21:33

Martel, S. J. and Boger, W. A. (1998). Geometry and mechanics of secondary fracturing around small three-dimensional faults in granitic rock. *J. Geophys. Res.*, **103**, 21 299–21 314.

Mastin, L. G. and Pollard, D. D. (1988). Surface deformation and shallow dike intrusion processes at Inyo Craters, Long Valley, California. *J. Geophys. Res.*, **93**, 13 221–13 235.

McGarr, A. and Gay, N. C. (1978). State of stress in the Earth's crust. *Ann. Rev. Earth Planet. Sci.*, **6**, 405–436.

McGill, G. E. (1993). Wrinkle ridges, stress domains, and kinematics of Venusian plains. *Geophys. Res. Lett.*, **20**, 2407–2410.

McGill, G. E. and Stromquist, A. W. (1979). The grabens of Canyonlands National Park, Utah: Geometry, mechanics, and kinematics. *J. Geophys. Res.*, **84**, 4547–4563.

McGill, G. E., Schultz, R. A., and Moore, J. M. (2000). Fault growth by segment linkage: An explanation for scatter in maximum displacement and trace length data from the Canyonlands Grabens of SE Utah: discussion. *J. Struct. Geol.*, **22**, 135–140.

Means, W. D. (1976). *Stress and Strain: Basic Concepts of Continuum Mechanics for Geologists*. New York, Springer-Verlag.

Mége, D. and Masson, P. (1996). Amounts of crustal stretching in Valles Marineris, Mars. *Planet. Space Sci.*, **44**, 749–782.

Mége, D. and Riedel, S. P. (2001). A method for estimating 2D wrinkle ridge strain from application of fault displacement scaling to the Yakima folds, Washington. *Geophys. Res. Lett.*, **28**, 3545–3548.

Mége, D., Cook, A. C., Garel, E., Lagabrielle, Y., and Cormier, M.-H. (2003). Volcanic rifting at Martian graben. *J. Geophys. Res.*, **108**, 5044, doi:10.1029/2002JE001852.

Molnar, P. (1983). Average regional strain due to slip on numerous faults of different orientations. *J. Geophys. Res.*, **88**, 6430–6432.

Moore, J. M. and Schultz, R. A. (1999). Processes of faulting in jointed rocks of Canyonlands National Park, Utah. *Geol. Soc. Am. Bull.*, **111**, 808–822.

Muehlberger, W. R. (1974). Structural history of southeastern Mare Serenitatis and adjacent highlands. *Proc. Lunar Sci. Conf.*, **5**, 101–110.

Neuffer, D. P. and Schultz, R. A. (2006). Mechanisms of slope failure in Valles Marineris, Mars. *Q. J. Eng. Geol. Hydrogeol.*, **39**, 227–240.

Neukum, G., Jaumann, R., Hoffmann, H., Hauber, E., Head, J. W., Basilevsky, A. T., Ivanov, B. A., Werner, S. C., van Gasselt, S., Murray, J. B., McCord, T., and the HRSC Co-Investigator Team (2004). Recent and episodic volcanic and glacial activity on Mars revealed by the High Resolution Stereo Camera. *Nature*, **432**, 971–979.

Nicol, A., Watterson, J., Walsh, J. J., and Childs, C. (1996). The shapes, major axis orientations and displacement patterns of fault surfaces. *J. Struct. Geol.*, **18**, 235–248.

Nimmo, F. and Schenk, P. (2006). Normal faulting on Europa: Implications for ice shell properties. *J. Struct. Geol.*, **28**, 2194–2203.

Niño, F., Philip, H., and Chéry, J. (1998). The role of bed-parallel slip in the formation of blind thrust faults. *J. Struct. Geol.*, **20**, 503–516.

Okubo, C. H. and Martel, S. J. (1998). Pit crater formation on Kilauea volcano, Hawaii. *J. Volcanol. Geotherm. Res.*, **86**, 1–18.

Okubo, C. H. and McEwen, A. S. (2007). Fracture controlled paleo-fluid flow in Candor Chasma, Mars. *Science*, **315**, 983–985.

Okubo, C. H. and Schultz, R. A. (2003). Thrust fault vergence directions on Mars: A foundation for investigating global-scale Tharsis-driven tectonics. *Geophys. Res. Lett.*, **30**, 2154, 10.1029/2003GL018664.

P1: aaa Trim: 174mm × 247mm Top: 0.553in Gutter: 0.747in
CUUK632-10 CUUK632-Watters ISBN: 978 0 521 76573 2 June 26, 2009 21:33

Okubo, C. H. and Schultz, R. A. (2004). Mechanical stratigraphy in the western equatorial region of Mars based on thrust fault-related fold topography and implications for near-surface volatile reservoirs. *Geol. Soc. Am. Bull.*, **116**, 594–605.

Okubo, C. H. and Schultz, R. A. (2006a). Near-tip stress rotation and the development of deformation band stepover geometries in mode II. *Geol. Soc. Am. Bull.*, **118**, 343–348.

Okubo, C. H. and Schultz, R. A. (2006b). Variability in Early Amazonian Tharsis stress state based on wrinkle ridges and strike-slip faulting. *J. Struct. Geol.*, **28**, 2169–2181.

Okubo, C. H., Schultz, R. A., Chan, M. A., Komatsu, G., and the HiRISE Team (2008a). Deformation band clusters on Mars and implications for subsurface fluid flow. *Geol. Soc. Am. Bull.*, **120**, in press.

Okubo, C. H., Lewis, K. L., McEwen, A. S., Kirk, R. L., and the HiRISE Team (2008b). Relative age of Interior Layered Deposits in southwest Candor Chasma based on high-resolution structural mapping. *J. Geophys. Res.*, **113**, E12002, doi:10.1029/2008JE003181.

Olson, J. E. (1993). Joint pattern development: Effects of subcritical crack growth and mechanical crack interaction. *J. Geophys. Res.*, **98**, 12 251–12 265.

Olson, J. E. (2003). Sublinear scaling of fracture aperture versus length: An exception or the rule? *J. Geophys. Res.*, **108**, 2413, doi:10.1029/2001JB000419.

Pappalardo, R. T. and Collins, G. C. (2005). Strained craters on Ganymede. *J. Struct. Geol.*, **27**, 827–838.

Paterson, M. S. and Wong, T.-F. (2005). *Experimental Rock Deformation: The Brittle Field*, 2nd edn. Berlin, Springer.

Peacock, D. C. P. (2002). Propagation, interaction and linkage in normal fault systems. *Earth-Sci. Rev.*, **58**, 121–142.

Peacock, D. C. P. (2003). Scaling of transfer zones in British Isles. *J. Struct. Geol.*, **25**, 1561–1567.

Peacock, D. C. P. and Sanderson, D. J. (1991). Displacement, segment linkage and relay ramps in normal fault zones. *J. Struct. Geol.*, **13**, 721–733.

Peacock, D. C. P. and Sanderson, D. J. (1993). Estimating strain from fault slip using a line sample. *J. Struct. Geol.*, **15**, 1513–1516.

Peacock, D. C. P. and Sanderson, D. J. (1995). Strike-slip relay ramps. *J. Struct. Geol.*, **17**, 1351–1360.

Peacock, D. C. P. and Sanderson, D. J. (1996). Effects of propagation rate on displacement variations along faults. *J. Struct. Geol.*, **18**, 311–320.

Plumb, R. A. (1994). Variations of the least horizontal stress magnitude in sedimentary basins. In *Rock Mechanics: Models and Measurements, Challenges from Industry*, ed. P. Nelson and S. E. Laubach. Rotterdam, Balkema, pp. 71–77.

Polit, A. T. (2005). Influence of mechanical stratigraphy and strain on the displacement-length scaling of normal faults on Mars. M. S. thesis, University of Nevada, Reno.

Polit, A. T., Schultz, R. A., and Soliva, R. (2009). Geometry, displacement-length scaling, and extensional strain of normal faults on Mars with inferences on mechanical stratigraphy of the Martian crust. *J. Struct. Geol.*, **31**, in press.

Pollard, D. D. and Fletcher, R. C. (2005). *Fundamentals of Structural Geology*. Cambridge: Cambridge University Press.

Pollard, D. D. and Segall, P. (1987). Theoretical displacements and stresses near fractures in rock: With applications to faults, joints, dikes, and solution surfaces. In *Fracture Mechanics of Rock*, ed. B. K. Atkinson. New York, Academic Press, pp. 277–349.

P1: aaa Trim: 174mm × 247mm Top: 0.553in Gutter: 0.747in
CUUK632-10 CUUK632-Watters ISBN: 978 0 521 76573 2 June 26, 2009 21:33

Poulimenos, G. (2000). Scaling properties of normal fault populations in the western Corinth Graben, Greece: Implications for fault growth in large strain settings. *J. Struct. Geol.*, **27**, 307–322.

Price, N. J. and Cosgrove, J. W. (1990). *Analysis of Geological Structures*. Cambridge, Cambridge University Press.

Priest, S. D. (1993). *Discontinuity Analysis for Rock Engineering*. New York, Chapman and Hall.

Ravnas, R. and Bondevik, K. (1997). Architecture and controls on the Bathonian Kimmeridgian shallow-marine syn-rift wedges of the Oseberg-Brage area, northern North Sea. *Basin Res.*, **9**, 197–226.

Reches, Z. (1978). Analysis of faulting in three-dimensional strain field. *Tectonophys.*, **47**, 109–129.

Reches, Z. (1983). Faulting of rocks in three-dimensional strain fields II. Theoretical analysis. *Tectonophys.*, **95**, 133–156.

Roberts, G. P., Cowie, P., Papanikolaou, I., and Michetti, A. M. (2004). Fault scaling relationships, deformation rates and seismic hazards: An example from the Lazio-Abruzzo Apennines, central Italy. *J. Struct. Geol.*, **26**, 377–398.

Rubin, A. M. (1992). Dike-induced faulting and graben subsidence in volcanic rift zones. *J. Geophys. Res.*, **97**, 1839–1858.

Rubin, A. M. and Pollard, D. D. (1988). Dike-induced faulting in rift zones of Iceland and Afar. *Geology*, **16**, 413–417.

Schenk, P. and McKinnon, W. B. (1989). Fault offsets and lateral crustal movement on Europa: Evidence for a mobile ice shell. *Icarus*, **79**, 75–100.

Schlische, R. W., Young, S. S., Ackerman, R. V., and Gupta, A. (1996). Geometry and scaling relations of a population of very small rift related normal faults. *Geology*, **24**, 683–686.

Scholz, C. H. (1997). Earthquake and fault populations and the calculation of brittle strain. *Geowiss.*, **15**, 124–130.

Scholz, C. H. (1998). Earthquakes and friction laws. *Nature*, **391**, 37–42.

Scholz, C. H. (2002). *The Mechanics of Earthquakes and Faulting*. 2nd edn. Cambridge: Cambridge University Press.

Scholz, C. H. and Cowie, P. A. (1990). Determination of total strain from faulting using slip measurements. *Nature*, **346**, 837–838.

Scholz, C. H. and Lawler, T. M. (2004). Slip tapers at the tips of faults and earthquake ruptures. *Geophys. Res. Lett.*, **31**, L21609, 10.1029/2004GL021030.

Scholz, C. H., Dawers, N. H., Yu, J.-Z., and Anders, M. H. (1993). Fault growth and fault scaling laws: Preliminary results. *J. Geophys. Res.*, **98**, 21 951–21 961.

Schultz, R. A. (1989). Strike-slip faulting of ridged plains near Valles Marineris, Mars. *Nature*, **341**, 424–426.

Schultz, R. A. (1991). Structural development of Coprates Chasma and western Ophir Planum, central Valles Marineris rift, Mars. *J. Geophys. Res.*, **96**, 22 777–22 792.

Schultz, R. A. (1992). Mechanics of curved slip surfaces in rock. *Eng. Anal. Bound. Elem.*, **10**, 147–154.

Schultz, R. A. (1993). Brittle strength of basaltic rock masses with application to Venus. *J. Geophys. Res.*, **98**, 10 883–10 895.

Schultz, R. A. (1995). Limits on strength and deformation properties of jointed basaltic rock masses. *Rock Mech. Rock Eng.*, **28**, 1–15.

Schultz, R. A. (1996). Relative scale and the strength and deformability of rock masses. *J. Struct. Geol.*, **18**, 1139–1149.

P1: aaa Trim: 174mm × 247mm Top: 0.553in Gutter: 0.747in
CUUK632-10 CUUK632-Watters ISBN: 978 0 521 76573 2 June 26, 2009 21:33

Schultz, R. A. (1997). Displacement-length scaling for terrestrial and Martian faults: Implications for Valles Marineris and shallow planetary grabens. *J. Geophys. Res.*, **102**, 12 009–12 015.

Schultz, R. A. (1999). Understanding the process of faulting: Selected challenges and opportunities at the edge of the 21st century. *J. Struct. Geol.*, **21**, 985–993.

Schultz, R. A. (2000a). Fault-population statistics at the Valles Marineris Extensional Province, Mars: Implications for segment linkage, crustal strains, and its geodynamical development. *Tectonophys.*, **316**, 169–193.

Schultz, R. A. (2000b). Localization of bedding plane slip and backthrust faults above blind thrust faults: Keys to wrinkle ridge structure. *J. Geophys. Res.*, **105**, 12 035–12 052.

Schultz, R. A. (2002). Stability of rock slopes in Valles Marineris, Mars. *Geophys. Res. Lett.*, **30**, 1932, 10.1029/2002GL015728.

Schultz, R. A. (2003a). A method to relate initial elastic stress to fault population strains. *Geophys. Res. Lett.*, **30**, 1593, 10.1029/2002GL016681.

Schultz, R. A. (2003b). Seismotectonics of the Amenthes Rupes thrust fault population, Mars. *Geophys. Res. Lett.*, **30**, 1303, 10.1029/2002GL016475.

Schultz, R. A. and Aydin, A. (1990). Formation of interior basins associated with curved faults in Alaska. *Tectonics*, **9**, 1387–1407.

Schultz, R. A. and Balasko, C. M. (2003). Growth of deformation bands into echelon and ladder geometries. *Geophys. Res. Lett.*, **30**, 2033, 10.1029/2003GL018449.

Schultz, R. A. and Fori, A. N. (1996). Fault-length statistics and implications of graben sets at Candor Mensa, Mars. *J. Struct. Geol.*, **18**, 373–383.

Schultz, R. A. and Fossen, H. (2002). Displacement-length scaling in three dimensions: The importance of aspect ratio and application to deformation bands. *J. Struct. Geol.*, **24**, 1389–1411.

Schultz, R. A. and Fossen, H. (2008). Terminology for structural discontinuities. *Am. Assoc. Petrol. Geol. Bull.*, **92**, 853–867.

Schultz, R. A. and Lin, J. (2001). Three-dimensional normal faulting models of Valles Marineris, Mars, and geodynamic implications. *J. Geophys. Res.*, **106**, 16 549–16 566.

Schultz, R. A. and Watters, T. R. (2001). Forward mechanical modeling of the Amenthes Rupes thrust fault on Mars. *Geophys. Res. Lett.*, **28**, 4659–4662.

Schultz, R. A. and Zuber, M. T. (1994). Observations, models, and mechanisms of failure of surface rocks surrounding planetry surface loads. *J. Geophys. Res.*, **99**, 14 691–14 702.

Schultz, R. A., Okubo, C. H., Goudy, C. L., and Wilkins, S. J. (2004). Igneous dikes on Mars revealed by MOLA topography. *Geology*, **32**, 889–892.

Schultz, R. A., Okubo, C. H., and Wilkins, S. J. (2006). Displacement-length scaling relations for faults on the terrestrial planets. *J. Struct. Geol.*, **28**, 2182–2193.

Schultz, R. A., Moore, J. M., Grosfils, E. B., Tanaka, K. L., and Mège, D. (2007). The Canyonlands model for planetary grabens: Revised physical basis and implications. In *The Geology of Mars: Evidence from Earth-Based Analogues*, ed. M. G. Chapman. Cambridge: Cambridge University Press, pp. 371–399.

Schultz, R. A., Soliva, R., Fossen, H., Okubo, C. H., and Reeves, D. M. (2008). Dependence of displacement-length scaling relations for fractures and deformation bands on the volumetric changes across them. *J. Struct. Geol.* **30**, 1405–1411.

Segall, P. (1984a). Formation and growth of extensional fracture sets. *Geol. Soc. Am. Bull.*, **95**, 454–462.

P1: aaa Trim: 174mm × 247mm Top: 0.553in Gutter: 0.747in
CUUK632-10 CUUK632-Watters ISBN: 978 0 521 76573 2 June 26, 2009 21:33

Segall, P. (1984b). Rate-dependent extensional deformation resulting from crack growth in rock. *J. Geophys. Res.*, **89**, 4185–4195.

Segall, P. and Pollard, D. D. (1980). Mechanics of discontinuous faults. *J. Geophys. Res.*, **85**, 4337–4350.

Segall, P. and Pollard, D. D. (1983). Joint formation in granitic rock of the Sierra Nevada. *Geol. Soc. Am. Bull.*, **94**, 563–575.

Sharpton, V. L. and Head, J. W. (1988). Lunar mare ridges: Analysis of ridge-crater intersections and implications for the tectonic origin of mare ridges. *Proc. Lunar Planet. Sci. Conf.*, *18*, 307–317.

Shaw, J. H., Plesch, A., Dolan, J. F., Pratt, T. L., and Fiore, P. (2002). Puente Hills blind-thrust system, Los Angeles, California. *Seismol. Soc. Am. Bull.*, **92**, 2946–2960.

Sibson, R. H. (1974). Frictional constraints on thrust, wrench and normal faults. *Nature*, **249**, 542–544.

Sibson, R. H. (1994). An assessment of field evidence for 'Byerlee' friction. *Pure Appl. Geophys.*, **142**, 645–662.

Soliva, R. and Benedicto, A. (2004). A linkage criterion for segmented normal faults. *J. Struct. Geol.*, **26**, 2251–2267.

Soliva, R. and Benedicto, A. (2005). Geometry, scaling relations and spacing of vertically restricted normal faults. *J. Struct. Geol.*, **27**, 317–325.

Soliva, R. and Schultz, R. A. (2008). Distributed and localized faulting in extensional settings: Insight from the North Ethiopian Rift – Afar transition area. *Tectonics*, **27**, TC2003, doi:10.1029/2007TC002148.

Soliva, R., Schultz, R. A., and Benedicto, A. (2005). Three-dimensional displacement-length scaling and maximum dimension of normal faults in layered rocks. *Geophys. Res. Lett.*, **32**, L16302, 10.1029/2005GL023007.

Soliva, R., Benedicto, A., and Maerten, L. (2006). Spacing and linkage of confined normal faults: Importance of mechanical thickness. *J. Geophys. Res.*, **110**, B01402, 10.1029/2004JB003507.

Solomon, S. C., McNutt, R. L., Jr., Watters, T. R., Lawrence, D. J., Feldman, W. C., Head, J. W., Krimigis, S. M., Murchie, S. L., Phillips, R. J., Slavin, J. A., and Zuber, M. T. (2008). Return to Mercury: A global perspective on MESSENGER's first Mercury flyby. *Science*, **321**, 59–62.

Sornette, A., Davy P., and Sornette, D. (1990). Growth of fractal fault patterns. *Phys. Rev. Lett.*, **65**, 2266–2269.

Suppe, J. (1985). *Principles of Structural Geology*. Englewood Cliffs, NJ, Prentice-Hall.

Suppe, J. and Connors, C. (1992). Critical-taper wedge mechanics of fold-and-thrust belts on Venus: Initial results from Magellan. *J. Geophys. Res*., **97**, 13 545–13 561.

Tchalenko, J. S. (1970). Similarities between shear zones of different magnitudes. *Geol. Soc. Am. Bull.*, **81**, 1625–1640.

Tse, S. T. and Rice, J. R. (1986). Crustal earthquake instability in relation to the variation of frictional slip properties. *J. Geophys. Res.*, **91**, 9452–9472.

Villemin, T. and Sunwoo, C. (1987). Distribution logarithmique self similaire des rejets et longueurs de failles: Exemple du bassin Houiller Lorrain. *Compte Rendu Acad. Sci., Série II*, **305**, 1309–1312.

Walsh, J. J. and Watterson, J. (1987). Distribution of cumulative displacement and seismic slip on a single normal fault surface. *J. Struct. Geol.*, **9**, 1039–1046.

Walsh, J. J. and Watterson, J. (1988). Analysis of the relationship between displacements and dimensions of faults. *J. Struct. Geol.*, **10**, 239–247.

Walsh, J. J., Watterson, J., and Yielding, G. (1991). The importance of small-scale faulting in regional extension. *Nature*, **351**, 391–393.

P1: aaa Trim: 174mm × 247mm Top: 0.553in Gutter: 0.747in
CUUK632-10 CUUK632-Watters ISBN: 978 0 521 76573 2 June 26, 2009 21:33

Walsh, J. J., Bailey, W. R., Childs, C., Nicol, A., and Bonson, C. G. (2003). Formation of segmented normal faults: A 3-D perspective. *J. Struct. Geol.*, **25**, 1251–1262.

Watters, T. R. (2003). Thrust faults along the dichotomy boundary in the eastern hemisphere of Mars. *J. Geophys. Res.*, **108**, 5054, 10.1029/2002JE001934.

Watters, T. R., Robinson, M. S., and Cook, A. C. (1998). Topography of lobate scarps on Mercury: New constraints on the planet's contraction. *Geology*, **26**, 991–994.

Watters, T. R., Schultz, R. A., and Robinson, M. S. (2000). Displacement-length scaling relations of thrust faults associated with lobate scarps on Mercury and Mars: Comparison with terrestrial faults. *Geophys. Res. Lett.*, **27**, 3659–3662.

Watters, T. R., Schultz, R. A., Robinson, M. S., and Cook, A. C. (2002). The mechanical and thermal structure of Mercury's early lithosphere. *Geophys. Res. Lett.*, **29**, 10.1029/2001GL014308.

Watterson, J. (1986). Fault dimensions, displacements and growth. *Pure Appl. Geophys.*, **124**, 365–373.

Weijermars, R. (1997). *Principles of Rock Mechanics*. Amsterdam: Alboran Science Publishing.

Weissel, J. K. and Karner, G. D. (1989). Flexural uplift of rift flanks due to mechanical unloading of the lithosphere during extension. *J. Geophys. Res.*, **94**, 13 919–13 950.

Wesnousky, S. G. (1994). The Gutenberg-Richter or characteristic earthquake distribution, which is it? *Seismol. Soc. Am. Bull.*, **84**, 1940–1959.

Wesnousky, S. G. (1999). Crustal deformation processes and the stability of the Gutenberg-Richter relationship. *Seismol. Soc. Am. Bull.*, **89**, 1131–1137.

Westaway, R. (1992). Seismic moment summation for historical earthquakes in Italy: Tectonic implications. *J. Geophys. Res.*, **97**, 15 437–15 464.

Westaway, R. (1994). Quantitative analysis of populations of small faults. *J. Struct. Geol.*, **16**, 1259–1273.

Wibberley, C. A. J., Petit, J.-P., and Rives, T. (1999). Mechanics of high displacement gradient faulting prior to lithification. *J. Struct. Geol.*, **21**, 251–257.

Wibberley, C. A. J., Petit, J.-P., and Rives, T. (2000). Mechanics of cataclastic 'deformation band' faulting in high-porosity sandstone, Provence. *Comptes Rendus Acad. Sci., Paris*, **331**, 419–425.

Wilkins, S. J. and Gross, M. R. (2002). Normal fault growth in layered rocks at Split Mountain, Utah: Influence of mechanical stratigraphy on dip linkage, fault restriction and fault scaling. *J. Struct. Geol.*, **24**, 1413–1429 (erratum, *J. Struct. Geol.*, **24**, 2007).

Wilkins, S. J. and Schultz, R. A. (2003). Cross faults in extensional settings: Stress triggering, displacement localization, and implications for the origin of blunt troughs in Valles Marineris, Mars. *J. Geophys. Res.*, **108**, 5056, 10.1029/ 2002JE001968.

Wilkins, S. J. and Schultz, R. A. (2005). 3D cohesive end-zone model for source scaling of strike-slip interplate earthquakes. *Seismol. Soc. Am. Bull.*, **95**, 2232–2258.

Wilkins, S. J., Schultz, R. A. Anderson, R. C. Dohm, J. M., and Dawers, N. C. (2002). Deformation rates from faulting at the Tempe Terra extensional province, Mars. *Geophys. Res. Lett.*, **29**, 1884, 10.1029/2002GL015391.

Willemse, E. J. M. (1997). Segmented normal faults: Correspondence between three-dimensional mechanical models and field data. *J. Geophys. Res.*, **102**, 675–692.

Willemse, E. J. M., Pollard, D. D., and Aydin, A. (1996). Three-dimensional analyses of slip distributions on normal fault arrays with consequences for fault scaling. *J. Struct. Geol.*, **18**, 295–309.

Williams, C. A., Connors, C., Dahlen, F. A., Price, E. J., and Suppe, J. (1994). Effect of the brittle-ductile transition on the topography of compressive mountain belts on the Earth and Venus. *J. Geophys. Res.*, **99**, 19 947–19 974.

P1: aaa Trim: 174mm × 247mm Top: 0.553in Gutter: 0.747in
CUUK632-10 CUUK632-Watters ISBN: 978 0 521 76573 2 June 26, 2009 21:33

Williams, M. L. (1957). On the stress distribution at the base of a stationary crack. *J. Appl. Mech.*, **24**, 109–114.

Wilson, L. and Head, J. W. (2002). Tharsis-radial graben system as the surface manifestation of plume-related dike intrusion complexes: Models and implications. *J. Geophys. Res.*, **107**, 5057, doi:10.1029/2001JE001593.

Wojtal, S. (1989). Measuring displacement gradients and strains in faulted rocks. *J. Struct. Geol.*, **11**, 669–678.

Zoback, M. D., Barton, C. A., Brudy, M., Castillo, D. A., Finkbeiner, T., Grollimund, B. R., Moos, D. B., Peska, P., Ward, C. D., and Wiprut, D. J. (2003). Determination of stress orientation and magnitude in deep wells. *Int. J. Rock Mech. Min. Sci.*, **40**, 1049–1076.